Bioactive Materials 30 (2023) 46–61

Contents lists available at ScienceDirect

Bioactive Materials

journal homepage: www.keaipublishing.com/en/journals/bioactive-materials

Collagen membrane functionalized with magnesium oxide via room-temperature atomic layer deposition promotes osteopromotive and antimicrobial properties

Soumya Saha [a], Raphael Cavalcante Costa [b], Mirela Caroline Silva [c], João Matheus Fonseca-Santos [c], Lin Chen [d], Abhijit H. Phakatkar [a], Harshdeep Bhatia [e], Leonardo P. Faverani [c], Valentim A.R. Barão [b], Tolou Shokuhfar [a], Cortino Sukotjo [f,**], Christos Takoudis [a,e,*]

[a] Department of Biomedical Engineering, University of Illinois Chicago, Chicago, USA
[b] Department of Prosthodontics and Periodontology, Piracicaba Dental School, University of Campinas (UNICAMP), Piracicaba, São Paulo, Brazil
[c] Department of Diagnosis and Surgery, Division of Oral and Maxillofacial Surgery and Implantology, São Paulo State University (UNESP), School of Dentistry, Araçatuba, São Paulo, Brazil
[d] Department of Periodontics, Center for Wound Healing and Tissue Regeneration, College of Dentistry, University of Illinois Chicago, Chicago, USA
[e] Department of Chemical Engineering, University of Illinois Chicago, Chicago, USA
[f] Department of Restorative Dentistry, University of Illinois Chicago College of Dentistry, Chicago, USA

A B S T R A C T

Artificial bone grafting materials such as collagen are gaining interest due to the ease of production and implantation. However, collagen must be supplemented with additional coating materials for improved osteointegration. Here, we report room-temperature atomic layer deposition (ALD) of MgO, a novel method to coat collagen membranes with MgO. Characterization techniques such as X-ray photoelectron spectroscopy, Raman spectroscopy, and electron beam dispersion mapping confirm the chemical nature of the film. Scanning electron and atomic force microscopies show the surface topography and morphology of the collagen fibers were not altered during the ALD of MgO. Slow release of magnesium ions promotes bone growth, and we show the deposited MgO film leaches trace amounts of Mg when incubated in phosphate-buffered saline at 37 °C. The coated collagen membrane had a superhydrophilic surface immediately after the deposition of MgO. The film was not toxic to human cells and demonstrated antibacterial properties against bacterial biofilms. Furthermore, *in vivo* studies performed on calvaria rats showed MgO-coated membranes (200 and 500 ALD) elicit a higher inflammatory response, leading to an increase in angiogenesis and a greater bone formation, mainly for Col-MgO500, compared to uncoated collagen. Based on the characterization of the MgO film and *in vitro* and *in vivo* data, the MgO-coated collagen membranes are excellent candidates for guided bone regeneration.

1. Introduction

Stimulation of healing of fractured bones is one of the most critical aspects of orthopedic surgery. Bone grafts are used to cure fractured bones by providing structural stability and linkage and stimulating osteogenesis [1]. Typically, a bone grafting material is defined as an implant material that, alone or in association with another material, promotes bone healing via osteogenic, osteoconductive, or osteoinductive activities at the implantation site [2]. Such materials are broadly classified into four categories: autograft, allograft, xenograft, and synthetic bone grafts. Out of these four, autografts are bone tissue materials harvested from the host body to be used on the same host and are osteogenic (viable cells), osteoinductive (matrix proteins), and osteoconductive (bone matrix). The use of autografts is limited due to the difficulty in harvesting. None of the remaining three has osteogenic properties, but good osteoconductive and osteoinductive properties may be expected depending on the material used and the type of application.

Collagen is abundant in animals and is an integral part of the bone, cartilage, skin, and tendon in humans [3]. Processed bovine collagen is biocompatible and used as xenografts in the form of gel, powder, sponge, paper, or matrices for several bone tissue engineering applications [2]. Type I collagen is one of the main constituents of the bone and

Peer review under responsibility of KeAi Communications Co., Ltd.
* Corresponding author. Department of Biomedical Engineering, University of Illinois Chicago, Chicago, USA.
** Corresponding author.
E-mail addresses: csukotjo@uic.edu (C. Sukotjo), takoudis@uic.edu (C. Takoudis).

https://doi.org/10.1016/j.bioactmat.2023.07.013
Received 1 March 2023; Received in revised form 2 July 2023; Accepted 17 July 2023

constitutes the natural scaffold. Commercially available collagen usually contains a mix of type I and III and has a bilayer structure [4]. Usually, collagen scaffolds or constructs are used in bone implants. However, collagen by itself suffers from delayed and insufficient osteointegration [5] and has poor mechanical strength and low fibrillar density [6]. To improve the osteointegration of collagen, collagen composites with hydroxyapatite were prepared [7]. Other techniques include incorporating bioactive glass [8] and surface coating using inorganic materials [9,10]. Surface coating was preferred due to the ease of implementation as a post-production technique.

Coating the surface with a thin film of inorganic materials can be done using different methods broadly categorized as liquid and vapor phase deposition methods. Out of which physical vapor deposition (PVD) and chemical vapor deposition (CVD) belong to vapor phase-based deposition techniques [11]. Liquid phase methods can involve processes like sol-gel [12,13], spin coating [14,15], and successive ionic layer adsorption and reaction (SILAR) [16] among others.

One of the disadvantages of using liquid phase deposition methods, in the case of collagen, is the exposure to solvents that can have an irreversible effect on its matrix [17–19]. Furthermore, these methods usually require drying at temperatures higher than 100 °C [14–16] to remove solvents, which can further degrade collagen substrate. Due to these limitations with liquid-based methods, vapor phase deposition methods were considered.

Out of the two, PVD typically requires high processing temperature and is not suitable for coating complex structures [20]. There have been many advances in PVD techniques, such as ion-beam assisted deposition (IBAD) [21,22] and RF sputtering [23], to allow lower deposition temperatures, but these usually involve the use of high energy sources which might damage the collagen structure [24,25]. In fact, IBAD of MgO has also been reported at room temperature on glass(SiO_2) substrates [22], however due to the well-documented damage ion beams can have on organic matter, it was not considered suitable. CVD also requires temperature higher than room-temperature and such processes are usually performed at 500–1100 °C [26]. Atomic layer deposition (ALD) is a superior version of CVD that deposits ultra-thin layers of metal or metal oxides that are conformal, uniform, and pin-hole free [11]. Recently, ALD has been used as a surface modification technique to functionalize dental implants for better osteointegration [20]. ALD typically requires 150–300 °C as the reaction temperature, but the literature includes many recent studies that achieved ALD films at a lower temperature [26–29]. This enables the use of temperature-sensitive materials such as collagen as the substrate, and the deposition of titania thin films at room temperature via ALD was previously reported by our group [30]. The deposited film was bioactive and enhanced the collagen material's biocompatibility by making it osteophilic [9]. However, all the metal and metal alloy-based implants show stress-shielding effects due to large differences in modulus of elasticity between the implant and that of the bone, and these materials must be removed via retrieval surgery [31].

Recently, Magnesium and magnesium alloy-based implants have attracted much attention because Mg can degrade in biological environments which eliminates the need for implant removal. Due to the corrosion of Mg implants in the presence of body fluids, Mg^{2+} ions are released, which promotes bone growth [32,33]. Magnesium is one of the essential micronutrients for the human body, being approximately 1% in the extracellular compartment, 50–60% in the bones, and around 30–35% in the intracellular compartment. Mg^{2+} ions enhance osteoblast and osteoclast activities, representing key co-factors for several enzymatic reactions in bone metabolism [34]. Zhang et al. fabricated hydrogels incorporated with Mg^{2+} and their study indicated that the modified hydrogels stimulate the osteogenic differentiation of Bone Mesenchymal Stem Cells and promotes angiogenesis [35]. Mg degradation led to the release of Mg2+ ions to surrounding tissue which resulted in the stimulation of local cells to promote bone growth due to the overall rate of seeded calcium phosphate crystallization, and the subsequent growth of hydroxyapatite [36,37], and significant increase in calcitonin gene-related polypeptide-α in bone fracture healing [38]. Another study also reported that Mg activates calcium ion channels on cells membrane and promote calcium deposition [39].

In the intracellular environment, Mg^{2+} cations are responsible for regulating various functions of cell signaling, cell growth, metabolism, and proliferation, thus being able to promote the differentiation of undifferentiated mesenchymal cells into osteoblasts, favoring bone neoformation [31–33].

Guided bone regeneration (GBR) is a principle to use a barrier to insulate the soft tissue flap from the tridimensional bone defects. Thus, a closed environment is formed allowing enough cells to the reconstructed area [7,8]. The barrier membranes should present favorable mechanical and biological properties, mainly biocompatibility, bioactive, tissue selectivity and antibacterial behavior [7]. Regarding the bioactivity property, it is related to osteogenic capacity of membranes. Recently, to improve the osteopromotive property of membranes in GBR, *in vitro* and *in vivo* studies have been adding some inorganic particles, growth factors, bone morphogenetic protein, and also biodegradable materials, such as Mg [9–11,20,26,27].

However, magnesium implants suffer from accelerated corrosion and release excess hydrogen gas as a toxic byproduct to the surrounding tissues. Excess corrosion leads to wear, bone loss, and implant failure [31,40,41]. Several fabrication techniques, alteration of alloying components, and surface modification of the Mg alloys have been attempted to reduce the corrosion rate [31,40,42]. The presence of secondary phases, larger grains, and non-uniform microstructure of the Mg alloys were found to be the contributing factors toward higher corrosion rate [43]. In this study, for the first time, magnesium oxide was deposited on collagen via ALD at room temperature. ALD of MgO at temperatures higher than room temperature on metal substrates was reported in the literature before [44,45]. We report the deposition of conformal, uniform, and amorphous magnesium oxide films on collagen with a high growth rate (~1.2 Å/cycle, measured on silicon) and the growth rate of magnesium oxide remained unchanged when the reaction temperature was lowered down to room temperature from 200 °C. In our study, 200 proof ethanol was used as an oxidizer due to the high reactivity of water with Magnesium and magnesium oxide [46][Ref from Soumya]. Furthermore, the use of water was not employed due to the effect of water in high vacuum systems, especially when at room temperature. Due to its negative Joule Thompson coefficient at room temperatures [47], water tends to stick to the walls of the ALD reactor which can lead to longer residence times and concomitant CVD [48]. Due to these disadvantages, water wasn't preferred for a low temperature ALD process. Our *in vivo* and *in vitro* data show that the MgO-coated collagen membranes possess osteoconductive and osteopromotive properties and can be excellent candidates for bone graft applications. Furthermore, the MgO coating is not cytotoxic and is shown to possess excellent antibacterial properties, generating cellular alterations in the bacteria, such as vacuolation, loss of contact and cell lysis, thus reducing the formation and adhesion of biofilms [49].

2. Materials and methods

2.1. ALD set up

Magnesium oxide was deposited using ALD in a patented custom-built hot wall reactor, and its early design was described in a previous article [50]. The ALD system has four precursor delivery lines and 1-s reactant delivery line (Fig. 1A); however, only one precursor line and the second reactant delivery lines were used for this project. The hot-wall ALD reactor is located downstream of the delivery lines. Bis (ethylcyclopentadienyl)magnesium (BECM), purchased from STREM Chemicals was used as the magnesium precursor. BECM was kept in a sealed metal bubbler and was heated to 50 °C to reach the required vapor pressure for ALD. Ar (99.99% Ar, Praxair) was used as the carrier gas for the precursor, which carried the precursor molecules to the

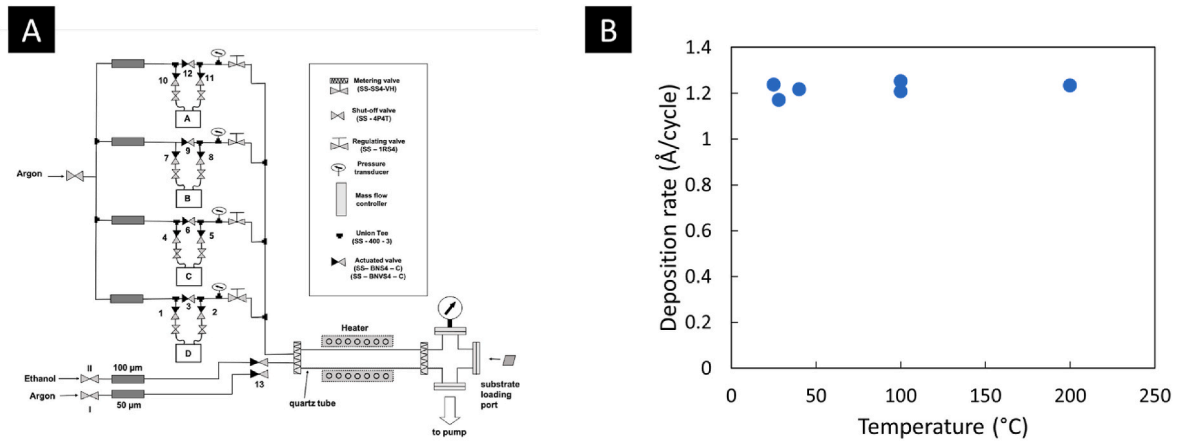

Fig. 1. Schematic drawing of the ALD system used and optimization of reaction temperature. **A)** Schematic of the custom ALD system show all four precursor delivery lines and the ethanol delivery line. Only one precursor delivery line was used for this project. **B)** Variation of the deposition rate of MgO with temperature over the range of 25–200 °C on Si. The plot shows the deposition rate remained consistent even at room temperature, provided all other ALD parameters were unchanged.

reactor in a flow-through manner at a flow rate of ~30 sccm. All delivery lines were kept at a higher temperature (70–80 °C) to prevent condensation of the precursor molecules. Anhydrous ethanol (200 proof, Decon Labs #2716) was used as the co-reactant and was supplied to the reactor using N_2 (99.99%, Praxair). Ethanol was kept in a sealed jacketed glass bubbler at room temperature for all experiments while N_2 was flowing through the bubbler. The approximate flow rate of N_2 mixed with ethanol vapor was 80 sccm upstream from the reactor. The collagen samples were cut into 2 × 2 cm^2 or smaller pieces and loaded on the quartz tube sample holder using a metal mesh. Details of collagen sample loading inside the reactor were described elsewhere [51]. Silicon wafers cut into ~1.5 × 1.5 cm^2 pieces were used as control during an ALD run. ALD was performed with 3 s of precursor pulsing followed by 20 s of Ar purging and 10 s of ethanol pulsing followed by 40 s of Ar purging for each cycle. Collagen samples were obtained from Zimmer under the brand BioMend® and BioMend® Extend™. Silicon substrates were <100>, p-type, highly doped, with resistivities of 1–5 Ω-cm (WaferPro, C04007). The ALD process was performed at ~450 mTorr pressure. Initially, the ALD was performed on Si samples at 200 °C, and the temperature was slowly decreased to room temperature. The ambient lab temperature was maintained at 25 °C. The deposition of MgO was checked at multiple temperature points, and it was found to be consistent at 1.2 Å/cycle over the range of 25–200 °C, irrespective of the selected temperature (Fig. 1B).

2.2. Characterization of the deposited MgO

Spectral ellipsometry (SE) (Model: M − 44, J.A. Woollam Co.) was used to measure the thickness of the MgO films deposited on Si. SE on collagen was ineffective as most of the incident light was absorbed by collagen, and the amount of transmitted light was below the detection limit. The MgO SE model was prepared using the materials files by comparing the goodness of fit between the experimental and the generated data. A Cauchy model was used to read MgO on Si that had thicknesses of Si and native SiO_2 added as layer 0 and layer 1, respectively. MgO was added as layer 2 from the J.A. Woollam materials files, and the thickness was determined for each sample by introducing polarized light at an incidence angle of 75°.

High-resolution scanning electron microscopy (SEM) was performed using Hitachi S4800 at × 35,000–40,000 magnification. Energy dispersive spectroscopy (EDS) was performed using Oxford's Ultim Max 100 mm^2 large-area silicon drift detector in the same instrument. Images were collected and processed using the bundled software.

Transmission electron microscopy (TEM) and scanning transmission electron microscopy with energy dispersive spectroscopy (STEM-EDS) elemental analyses of MgO deposited collagen fiber were performed using aberration-corrected JEOL ARM200CF atomic resolution (200 kV) scanning transmission electron microscope. The sample suspension was obtained by scratching a top layer of MgO thin film deposited on collagen fibers using a surgical scalpel, followed by dispersing in an isopropyl alcohol solvent and sonicating for 10 min 2 μL solution suspension of dispersed MgO deposited collagen fibers were drop casted on lacey carbon-coated copper TEM grid for STEM-EDS analysis. STEM-EDS analysis of collagen fibers was performed at 5X probe size, and elemental spectra were obtained using the Oxford EDS system tuned with a drift corrector and 5 μs acquisition time per pixel. High-angle annular dark field (HAADF)-STEM image was acquired using 512 × 512 pixels scanning resolution with a 22 mrad convergence angle.

Atomic force microscopy (AFM) (Model: Alpha300 RA, WITec) was performed on samples over a 15 × 15 μm area to determine topography. The software Gwyddion [52] was used to analyze the AFM data. Mean roughness (S_a), which corresponds to the irregularities in heights on the surface and the one-dimensional roughness parameter, root mean square roughness (R_q: the average of measured height deviations from the mean along the line of measurement) were determined using the tools provided by the software. The same instrument was used to perform Raman spectroscopy, and the magnesium peaks were identified in the spectra.

X-ray photoelectron spectroscopy (XPS) was performed on MgO-coated collagen substrates for elemental analysis. However, high-resolution scans around Mg 2p on collagen were also performed. Kratos AXIS-165, Kratos Analytical Ltd. was used for XPS analysis with a monochromatic Al Kα X-ray source. Survey scans were performed with a dwell time of 100 ms, an emission current of 15 mA, a pass energy of 80 eV, and a step size of 1 eV. The parameters were changed to a dwell time of 800 ms, a pass energy of 20 eV, and a step size of 0.1 eV for the high-resolution scans. The electron emission angle was always kept at 90° for all XPS scans performed. The 'spot size' or the size of the analyzed area was 1150 × 700 μm. Pressure in the X-ray acquisition chamber was $<5 \times 10^{-10}$ torr with the X-ray off and $<8 \times 10^{-9}$ torr with the X-ray on. The peaks were identified and annotated using CasaXPS [53].

The tensile strength of collagen control and MgO-coated membranes was tested using a motorized tensiometer (Mark-10, Copiague, NY). The tensiometer had a range of 0–5 lbf (0–22.24 N) with a resolution of 0.002 lbf (0.009 N). The collagen control and as-deposited samples were cut into strips of 2.5 mm × 15 mm and clamped in the tensiometer jaws using thumbscrews. The distance between the clamps was kept at a constant value of 5 mm. The thin strips were then stretched at a constant

rate of 150 mm/min until tearing occurred. The load required to tear the membrane was then converted to tensile strength using equation (1) where an average thickness of 0.2 mm measured using a micron-gauge (Mitutoyo America Corp., Aurora, IL) was used,

$$\sigma = \frac{F}{C.S.A} \quad (1)$$

where, σ = Tensile strength (MPa), F = Tearing load (N) C.S.A = cross sectional area (mm^2).

Inductively coupled plasma mass spectroscopy (ICP-MS) was performed on non-coated (control) and MgO-coated collagen samples using NexION 350D (PerkinElmer Inc.). The samples were subjected to acid digestion to determine the amount of Mg on the coated samples. The control and coated samples were incubated in phosphate-buffered saline (PBS) solution for 1, 2, and 4 weeks at 37 °C, and the extracts were analyzed via ICP-MS to observe the rate of leeching of Mg^{2+} ions into the solution over each time period chosen.

2.3. Assessment of anti-bacterial property, WCA and cell viability of the MgO-coated membranes

The antibacterial activity of Mg-loaded membranes was tested against polymicrobial biofilm from human saliva, following a previous protocol [54]. For this, a pool of fresh stimulated human saliva from three healthy donors was used as a microbial inoculum to mimic the human oral microbiome [55,56]. All protocols were reviewed and approved by the University Research and Ethics Committee (protocol 86638918.0.0000.5418). Initially, samples (∅ 5 mm; 2 independent experiments, n = 3/experiment) were cleaned by UV-light (4 W, λ = 280 nm, Osram Ltd., Berlin, Germany) for 20 min. Then, samples [Col (control); Col-MgO200 and Col-MgO500 (experimental)] were incubated with the salivary microbial inoculum (~10^7 cells/mL) in the BHI medium (Becton-Dickinson, Sparks, MD, USA) (10:1 v/v) for 2 h to promote initial microbial adhesion at 37 °C with 10% CO_2. At the same time, samples (n = 6 per group) were also incubated in BHI medium + saliva inoculum for 24 h at 37 °C with 10% CO_2. Finally, the samples were transferred to cryogenic tubes with 1 mL of 0.9% NaCl, vortexed for 10 s, and then sonicated (7 W for 30 s) (S 150D, Branson Ultrasonics Corp., Danbury, CT) to detach cells from the surface. An aliquot of 100 μL of the sonicated suspension was sequentially diluted 6-fold in 0.9% NaCl. Two drops of 20 μL of each dilution were plated on Columbia Blood Agar (CBA) for the colony-forming unit (CFU) counts. Data of CFU were normalized from the control group, which was set to 100%, to reduce the effect of differences in biofilm accumulation among the samples [57]. SEM was performed to analyze the structure of the polymicrobial biofilms formed on the Col, Col-MgO200, and Col-MgO500 surfaces (n = 1 per group). The biofilm was fixed in Karnovsky's fixation solution (2% formaldehyde, 2.5% glutaraldehyde, 0.1 M sodium phosphate buffer; pH 7.2) for 2 h. Next, the samples were serially dehydrated in ethanol washes and then allowed to dry. (37) Finally, the samples were gold-sputtered and visualized by SEM (JSM5600LV, JEOL USA, Inc., Peabody, MA) operating at 15 kV [58].

The wetting behavior of the MgO coating was analyzed using a static water droplet contact angle (WCA) measurement method using a contact angle goniometer (Model 100−00, Ramé-Hart Instrument Co.) WCA measurements were taken immediately after ALD and after 14 days post deposition.

For cell proliferation assay, a total of 10^3 human telomerase immortalized gingival keratinocytes (TIGK, ATCC, Manassas, VA) per well were seeded in a 96-well plate with or without 6 mm in diameter Col (control), Col-MgO200, and Col-MgO500 membranes in 200 μl serum-free culture medium (DermaLife K Medium Complete Kit, Lifeline Cell Technology) with antibiotics of penicillin (100U/ml) and streptomycin (100μ/ml). Before plating the cells on the membranes, each side of the membranes was sterilized by radiation under the UV for 60 min in a Bio Safety Cabinet. Cells were cultured in an incubator at 37 °C in a 5% CO_2 environment. A cell proliferation assay on days 1 and 5 was performed using a colorimetric MTS Assay Kit (Abcam, Waltham, MA). Briefly, 20 μl of MST solution was added to each well on days 1 and 5. The optical density (OD) at 490 nm was read using a spectrophotometer (SPECTRAmax Plus, Molecular Devices, San Jose, CA) after 1-h incubation.

2.4. In vivo analysis of the MgO-coated membranes

2.4.1. Ethics statement

This study was approved by the ethical committee for the use of animals from the São Paulo State University (UNESP), School of Dentistry, Aracatuba – SP, Brazil (Protocol number: 0646–2022), which followed the ARRIVE guidelines in animal studies [59]. Thirty-nine Wistar rats (*Rattus norvegicus*), ranging from 250 to 300 g of weight, male and adult (six months of age), were selected for this study; among which thirty-six were for critical-size defect analyses, and the remaining three were for biocompatibility analysis. All animals were kept at the vivarium with four animals per cage with controlled temperature (22 ± 2 °C), light cycle (12 h of light and 12 h of dark) and provided solid food and water *ad libitum*.

2.4.2. Surgical experimental design and groups

Thirty-six animals were subjected to a bilateral calvaria critical-size defect and divided into five groups: 1) Blood clot – BC (negative control group): the bone defects were not covered by any membranes, but only with blood clot from the bone stumps; 2)Collagen Membrane – Col (positive control group): the bone defects were covered by uncoated collagen membrane; 3) Collagen Membrane with 200 ALD cycles of MgO – Col-MgO200: the bone defects were covered by coated membranes with 200 ALD cycles of MgO; 4) Collagen Membrane with 500 ALD cycles of MgO – Col-MgO500: the bone defects were covered by coated membranes with 500 ALD cycles of MgO. The three remaining animals received the three membranes analyzed (Col, Col-MgO200, and Col-MgO500) in the subcutaneous for biocompatibility analysis.

2.4.3. Critical size defect assay

The animals were sedated using intramuscular ketamine (50 mg/kg) and xylazine (5 mg/kg), Trichotomy was performed on the calvaria area between the eyes and nose. The antisepsis was performed using degermant and topic Polyvinyl Pyrrolidone Iodine (PVPI). A V-incision was designed, and the flap was detached with the apex located in the frontal region. A 5-mm bone defect was performed on each side of the parietal bone, maintaining the integrity of the dura mater. The bone defects were covered following the experimental groups (BC, Col, Col-MgO200, and Col-MgO500), randomly allocated. Flap suture was done using Nylon 5.0 (Mononylon, Ethicon, Johnson Prod., São José dos Campos, Brazil). All animals received a single dose of 0.2 mL of Pentabiotic® - Intramuscular injection (Pentabiótico Veterinário Pequeno Porte, Fort Dodge Saúde Animal Ltda., Campinas, SP). Animals were euthanized at 7, 14, and 28 days postoperatively. The samples from 7 to 14 days were subjected to histology/histometric and immunohistochemical analyses, and those from 28 days, were used for microtomography, and histology/histometric analyses.

2.4.4. Biocompatibility analysis

The same sedative and anesthetic protocols were applied to these animals. After trichotomy, three linear incisions with 2 cm were performed on the back of the rats [two on the cranial region (one on the left region, and one on the right region), and one on the right caudal region]. Thus, all animals received the three membranes (Col; Col-MgO200; Col-MgO500) and distributed randomly. The membranes were stabilized in the subcutaneous tissue through a monofilament suture (Nylon 5.0, Mononylon, Ethicon, Johnson Prod., São José dos Campos, Brazil). The same postoperative protocol was applied. Animals were euthanized at 3

postoperative days, and the soft tissue surrounding membranes was collected to assess the inflammation process.

2.4.5. Assessment

After euthanasia and collection of samples (calvaria and subcutaneous tissue), they were maintained in formol for 48 h and followed by all of the lab steps to include in paraffin (decalcification in Ethylenediaminetetraacetic acid (EDTA) for 8 weeks, diaphanization in Xylol, and the blocks were obtained using paraffin for inclusion).

2.5. Critical size defect assay

2.5.1. Computed microtomographic (micro-CT) analysis

The samples obtained at 28 days were scanned by a SkyScan microtomography (SkyScan 1176 Bruker MicroCT, Aatselaar, Belgium, 2003), using the following parameters: 8-μm sections, 90 Kv, 111 μA, with copper and aluminum filters and a 0.05-mm rotation pitch. The images were reconstituted with NRecon software (SkyScan, 2011; Version 1.6.6.0); image reconstruction and position were performed in the Data Viewer software (SkyScan, Version 1.4.4 64-bit). CT-An software (SkyScan, 2012 Bruker MicroCT, Version 1.12.4.0) was used to define the interest area (bone defect), which was analyzed separately. Therefore, the parameters BV.TV - percentage of bone volume, Tb.Th - bone trabecular thickness, Tb.SP - separation of bone trabeculae, and Tb.N - number of trabeculae were obtained to assess the bone tissue quantity and quality.

2.5.2. Inflammatory cells and blood cells count

The histological blades were stained with hematoxylin and eosin (HE). The inflammatory cell count was performed, emphasizing lymphocytes and vessels. The blades were photographed using a light microscope (DM 4000B, Leica) and the ImageJ software (National Institutes of Health, Bethesda, MD, USA) was used for data quantification. For the image quantifying, an objective of × 100 magnification was used, and a grid with 130 points was applied to allow the count of cells.

2.5.3. Bone formed

The same blades were used for analyzing bone formation and photomicrographed in a × 6.3 magnification (DM 4000B, Leica). The central area of the bone tissue of each bone defect was evaluated. On average, 15 pictures were taken for each defect, and then those images were displaced to the Adobe Photoshop CC 2019 to merge into a panoramic view. Then, using the tool "free hands'' in the ImageJ software, the bone-formed area was measured directly in the central region of the calvaria defect during the bone healing process.

2.5.4. Residual membrane area

The images, also in a panoramic view were analyzed in the ImageJ program, using the "free hands" tool to quantify the area of residual membrane in pixels^2.

2.5.5. Residual linear defect

The images in the Image J program were analyzed by the "straight" tool to measure residual linear defects. The amount of closure defect was calculated linearly.

2.5.6. Biocompatibility analysis

For the analysis of subcutaneous behavior surrounding the membranes, the blades were photographed using an objective of × 100 magnification. In the Image J software, a grid with 130 points was applied to allow the count of inflammatory cells, emphasizing lymphocytes.

3. Results and discussion

3.1. Characterization of the deposited MgO on collagen

SEM was performed on uncoated collagen (Col), collagen after 200 ALD cycles of MgO ('Col-MgO200' in Fig. 2), and collagen after 500 ALD cycles of MgO ('Col-MgO500' in Fig. 2). Repeated cross-linking patterns can be seen with lower-resolution SEM imaging on all three samples. Pictures of membranes with and without the MgO coating are presented in Fig. 2A. No significant changes were noticed after the deposition besides slight changes of the color from white to yellowish due MgO deposition. More regular patterns were observed on the 500 sample as ALD conformally coated the substrate with MgO (Fig. 2B). With high-magnification imaging, striation on the collagen fibers can be seen on the control samples. The fibers had varying diameters and were closely packed. The fibers got thicker with the increasing number of ALD cycles, and striation in the individual fibers was not observed on the coated samples (Fig. 2C). The data obtained are consistent with the observations made on TiO_2-coated collagen membranes in a prior study [9]. In addition, EDS (energy dispersive X-ray spectroscopy) mapping was performed on all three samples. Carbon, oxygen, and nitrogen are the main constituents of protein, and all three elements were observed in all samples. A strong magnesium signal was observed on both Col-MgO200 and Col-MgO500 samples, the latter having a higher relative amount of Mg as expected. The selected elements were mapped on the micrographs themselves, and the intensity of the color was directly proportional to the relative amount of that element present in the sample. TEM (transmission electron microscopy) was performed on Col-MgO500 ALD cycles of MgO. Fig. 2D shows a high-angle annular dark field (HAADF) image of MgO and STEM-EDS analysis of the deposited film on a single collagen fiber acquired using aberration-corrected scanning transmission electron microscope. Fig. 2E shows STEM-EDS relative peak intensities of the elements detected on Col-MgO500 and individual elemental mapping confirming the homogeneous presence of characteristic carbon (C), oxygen (O), nitrogen (N), and magnesium (Mg) elements along the length of the collagen fiber. STEM-EDS elemental mapping of carbon consists of a signal from a MgO deposited collagen fiber in addition to an amorphous carbon layer from a lacey carbon copper TEM grid. STEM-EDS elemental mapping clearly confirms the uniform deposition of the MgO layer on collagen fiber. In the HAADF-STEM image, based on the elemental atomic number-based diffraction contrast principles, collagen fibers composed of C, O, and N elements appear in lighter contrast, while MgO deposited film attributed to mainly Mg element appears in the brighter contrast. Respective C and N STEM-EDS elemental maps signify the central region associated with collagen fibers.

Atomic force microscopy (AFM) was used to study the surface topography of the coated and control collagen samples. ALD being a conformal deposition technique, was expected to coat the collagen fibers uniformly and retain the topography of the uncoated collagen samples. The AFM scans performed on Col, Col-MgO200, and Col-MgO500 samples are shown in Fig. 3. Col had a wavy topography due to the fibrous nature of the sample, and the measured roughness (R_q) was $0.9 \pm 0.3\ \mu m$ (Fig. 3A, A′). The Col-MgO200 and Col-MgO500 samples retained the original wavy topography of the collagen membrane. However, it can be observed from Fig. 3B, B′ and **3C, 3C'** that the roughness matches the texture of the surface. This happens due to the conformal nature of the MgO coating. Also, the R_q values were lower for both coated samples ($0.15 \pm 0.07\ \mu m$ for Col-MgO200 and $0.5 \pm 0.09\ \mu m$ for Col-MgO500). XPS survey spectra were performed on control and coated samples as qualitative analysis to validate the presence of Mg on the surface. Mg 1s (~1304 eV), 2s (~89 eV), and 2p (~51 eV) peaks were identified on the MgO-coated collagen samples (Fig. 3D). The Auger peak Mg KLL was also observed. O 1s, N 1s, and C 1s were seen on all three samples at approximately 532 eV, 398 eV, and 285 eV, respectively. The position of

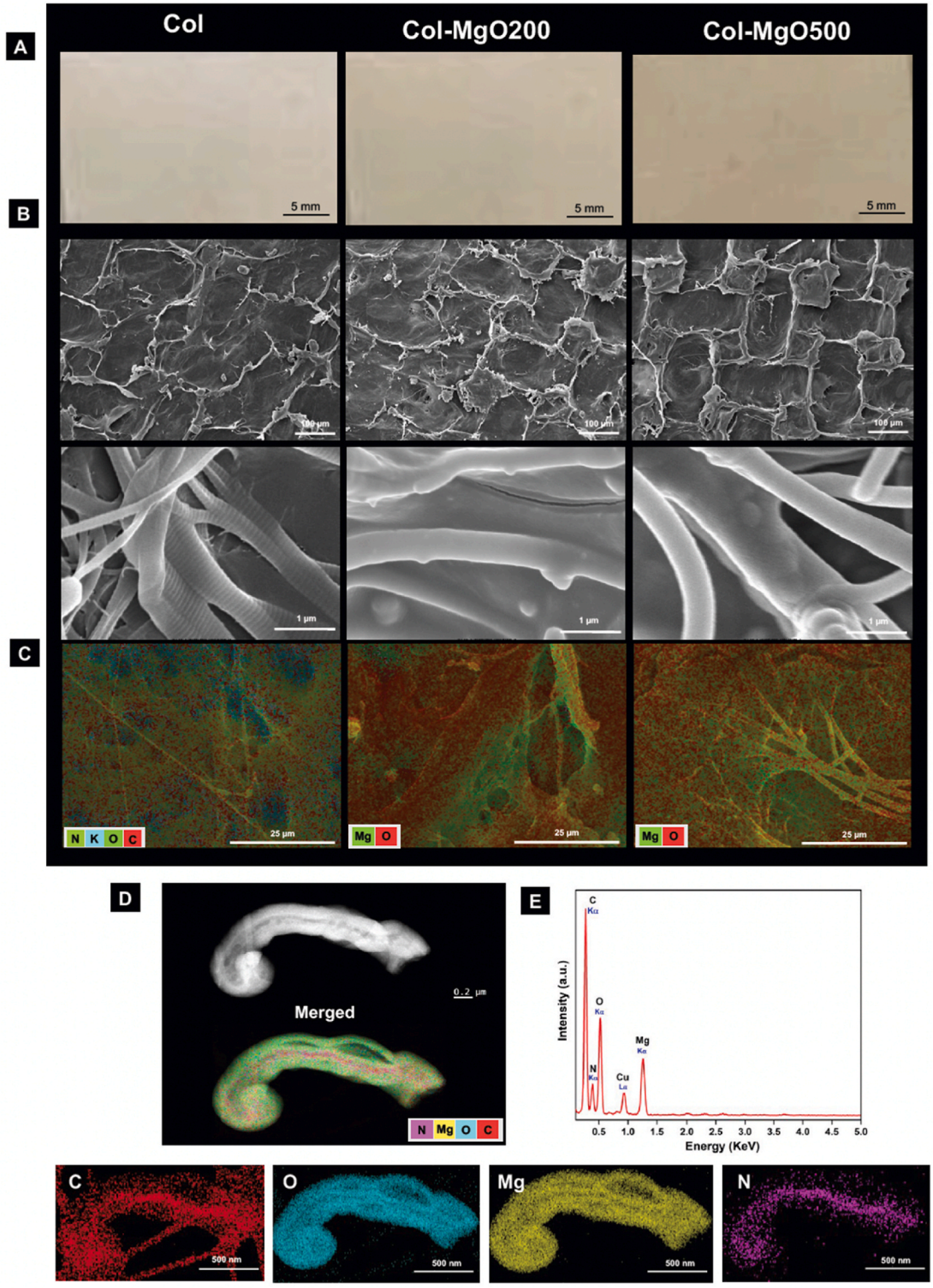

Fig. 2. 'Col', 'Col-MgO200', and 'Col-MgO500' correspond to uncoated collagen membrane, collagen after 200 ALD cycles of MgO, and collagen after 500 ALD cycles of MgO coating, respectively. **A)** General pictures of membranes with and without the MgO coating. No significant changes were noticed after the deposition besides slight changes of the color from white to yellowish due MgO deposition. **B)** SEM images of collagen fibers with and without the MgO coating. Lower (top) and higher (bottom) resolution micrographs: more regular patterns are observed with an increasing number of ALD cycles in the lower resolution images. Striations are observed in Col, which are absent in the Col-MgO200 and Col-MgO500 samples in the high-resolution images. **C)** EDS mapping, performed on the high-resolution images, shows the presence of nitrogen, oxygen, and carbon. Magnesium was observed on both Col-MgO200 and Col-MgO500. The intensity of the color green selected for Mg in EDS mapping directly corresponds to the relative amount of Mg present in the samples. **D)** HAADF-STEM micrograph and corresponding STEM-EDS elemental mapping of Col-MgO500 deposited collagen fiber. **E)** EDS spectrum and STEM-EDS elemental mapping showing the relative intensities and uniform distribution of carbon, oxygen, nitrogen, and magnesium elements along the length of MgO-deposited collagen fiber. Both SEM and TEM analyses performed on the samples showed the deposited film uniformly coated the collagen fibers without altering the chemical nature and physical morphology of the collagen membrane. The deposited film was amorphous and free from any secondary phase or grains.

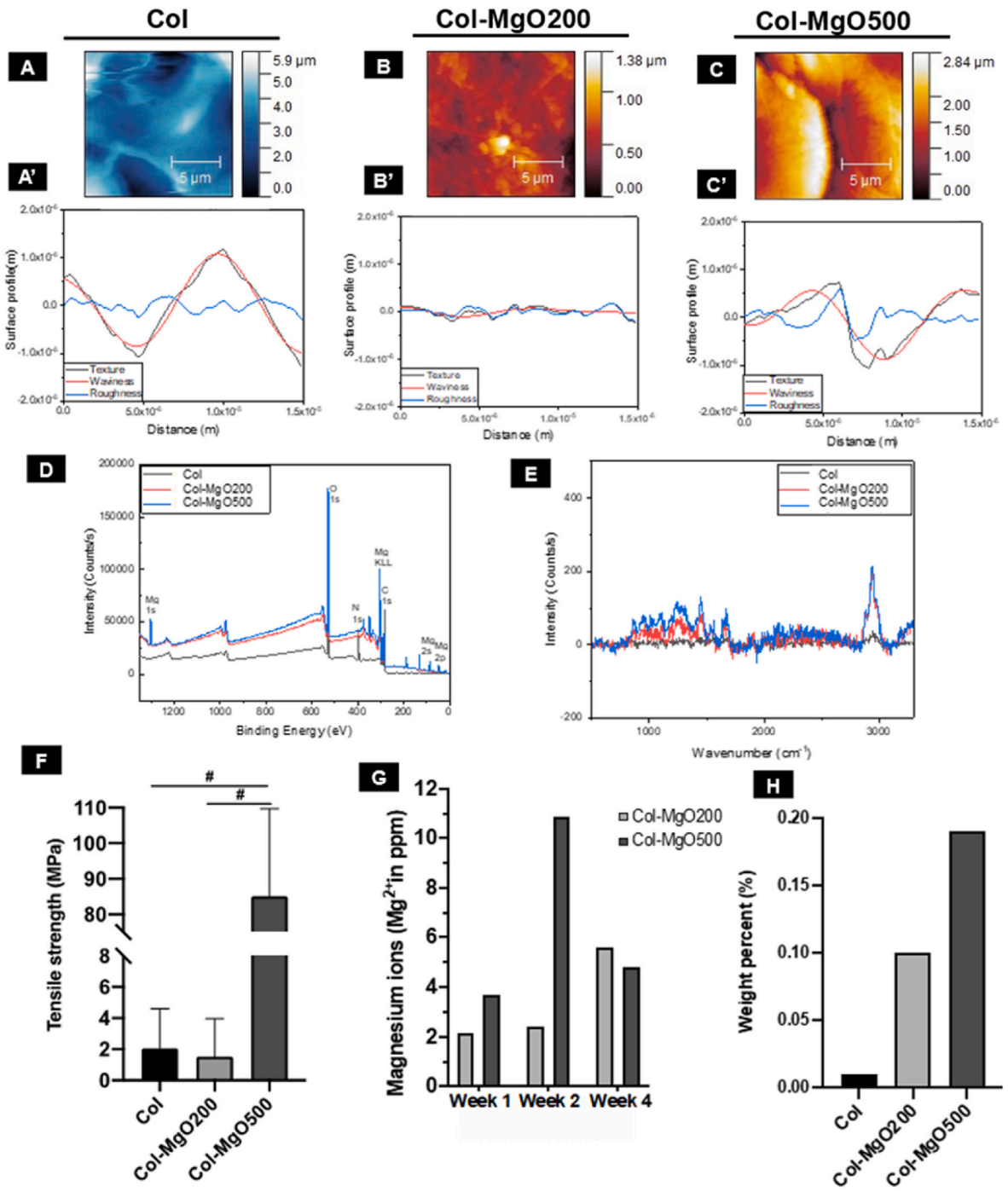

Fig. 3. Additional surface characterization and analysis of the degradation rate of MgO performed on Col, Col-MgO200, and Col-MgO500 samples. **A-C)** 2D AFM images of Col, Col-MgO200, and Col-MgO500 samples respectively. **A′)** Col shows a wavy surface topography with low surface roughness which is expected due to the fibrous nature of the sample. **B′)** Col-MgO200 retains the wavy nature, but surface roughness matches with the texture as ALD conformally coats the surface. **C′)** Surface texture of Col-MgO500 matches the roughness profile while preserving the surface topography of Col. **D)** Overlay of survey spectra collected on all three samples. Mg peaks (1s, 2s, and 2p) along with the Auger KLL were seen on both coated collagen samples. N 1s peak is prominent only on the control sample indicating the MgO coating covers the entire surface. **E)** Overlay of Raman spectra collected on all three samples. The peaks below 1500 cm^{-1} belong to *D*-band, and the peaks at 1500 and 3000 cm^{-1} are associated with *G*-band. **F)** Tensile strength of control Col, Col-MgO200 and Col-MgO500 samples collected using strips of size 2.5 mm × 15 mm x 0.2 mm (n = 6) **G)** ICP-MS analyses performed on PBS extracts incubated with Col-MgO200 and Col-MgO500 samples for 1 week, 2 weeks, and 4 weeks respectively. **H)** ICP-MS analyses performed on acid-digested Col, Col-MgO200, and Col-MgO500 samples.

these peaks is identical to those observed on TiO_2-coated collagen in a prior study [9]. N 1s peak is sharp on control collagen but is barely visible on the coated samples, which can be attributed to the fact that the film was thick enough to cover the entire surface. High resolution XPS of Mg2p was performed on collagen samples after 200 cycles of ALD to identify the chemical state of the coated film. This has been given in the supplementary information along with the XPS spectra for MgO given in previous literature [60]. This revealed a peak located at 49.5 eV; however, this was a broad peak and peak deconvolution revealed two separate peaks at 49.45 ± 0.21 eV and 51.24 ± 0.26 eV which were attributed to the oxides and hydroxides of magnesium respectively [60,61]. Additionally, STEM-EDS elemental mapping further shows that

nitrogen is only present at the core while magnesium signal was found all around; thus, the coating was conformal in nature. Raman spectroscopy performed on the samples showed *D*-band and *G*-band Mg peaks on the coated samples (Fig. 3E). The positions of these peaks are consistent with the previously reported positions in the literature [62].

Fig. 3F compares the tensile strength of all collagen samples. The tensile strength of the collagen samples with 200 cycles of MgO ALD was calculated as 1.51 MPa with a standard deviation of 2.4 MPa. This was close to the control sample's tensile strength of 2.05 ± 2.5 MPa and values previously reported for different collagen membranes [63] and BioMend membrane [64]. However, a significant increase was observed after 500 cycles of MgO ALD, where the average tearing load increased to 17.03 N, with a resultant tensile strength of 85 ± 25 MPa (Fig. 3F). Different techniques have been successfully used to modify the intrinsic and extrinsic tensile properties of collagen either by mineralization with solutions of calcium and phosphate ions [65,66] or cross-linking with organic molecules such as chitosan or catechins [67,68]. Other techniques, such as bilayer/composites with gelatin alginate have also been used to modify collagen tensile strength [69]; however, the maximum tensile strength achieved by these methods was about 10 MPa for a crosslinking study [67]. ALD, albeit a slow process, is a post-production technique that requires little modification to existing production techniques, a feature that would be missing in some strategies of surface functionalization. Previously, ALD was used to deposit TiO_2 film to collagen membrane and increased its tensile strength from ~305 MPa to ~385 MPa [70]. Seung-Mo Lee also reported the use of low temperature ALD to infiltrate metal/metal oxide into biomaterials such as spider silk [71], egg shell [72] and collagen membrane [73].This infiltration process caused significant changes to material composition and the protein structures, which leads to enhanced mechanical properties [71–73].

Inductively coupled plasma mass spectroscopy (ICP-MS) is a high-precision technique to determine the presence or absence of certain elements. A two-pronged approach was taken in order to effectively apply this technique to our study. Initially, acid digestion was performed on Col, Col-MgO200, and Col-MgO500 samples to assess the amount of magnesium present. Fig. 3H compares the amount of Mg present among all three samples in weight percent. The trace amount of Mg detected in the control was determined to be an environmental impurity, as the presence of Mg in the control was not detected via SEM or TEM analyses. Mg is osteoconductive and osteoinductive [74] and controlled release of Mg^{2+} ions promote bone growth [75]. Thus, it was essential to determine whether Mg^{2+} ions could be released over time from the deposited MgO films. PBS has been used in *in vitro* corrosion studies of magnesium implants [76]. In our study, the Col-MgO200 and Col-MgO500 samples were incubated in PBS solution at 37 °C to resemble the environment inside a human body. Fig. 3G shows the concentration of Mg^{2+} leached into PBS for these samples over the intervals of 1 week, 2 weeks, and 4 weeks. A steady increase in Mg^{2+} concentration can be observed in the case of Col-MgO200 from week 1 (2.16 ppm) to week 4 (5.6 ppm). However, for Col-MgO500, the highest concentration of leached Mg^{2+} was observed after week 2 (10.87 ppm). At week 4, the extract from Col-MgO200 had a higher concentration (5.6 ppm) of Mg^{2+} than that of Col-MgO500 (4.79 ppm). In the case of magnesium implants, MgO is readily formed due to the interaction of the surface with air and moisture and is less corrosive than pure Mg [77]. This oxide layer is hydrophilic and forms magnesium hydroxide in the presence of water. Higher solubility of MgO than that of $Mg(OH)_2$ causes supersaturation of the surface with water leading to precipitation of $Mg(OH)_2$ [78]. The magnesium hydroxide layer formed on the surface provides additional protection against corrosion, and the presence of a thicker MgO may allow the formation of a thicker $Mg(OH)_2$ layer when incubated in an aqueous environment. However, $Mg(OH)_2$ was precipitated only on the surface, and the presence of impurities and difference in an oxidation state of Mg throughout the bulk material caused the continuation of localized corrosion [77]. In our study, the deposited film was MgO-free from any metal impurity. Precipitation of $Mg(OH)_2$ in PBS during longer incubation time is highly probable on Col-MgO500 samples due to the higher thickness of the film. The hydroxide layer would provide additional protection against corrosion and lower the release of Mg^{2+} in the solution.

3.2. In vitro studies

The antibacterial activity of Mg-loaded membranes was determined by CFU (See Supplementary Material) and checked by relative biofilm formation percentual (Fig. 4A). There seems to be a possible antibacterial effect on late polymicrobial biofilm formation (~1.5-log killing). In fact, relative biofilm formation on Mg-loaded membranes was significantly lower when compared with non-coated collagen membranes ($p < 0.05$) after 24 h of biofilm growth. Col-MgO200 and Col-MgO500 reduced bacterial viability by ~20% and ~25%, respectively. Additionally, no differences were found between Col-MgO200 and Col-MgO500 ($p > 0.05$), suggesting a limited dose-dependent effect. Therefore, the mechanism behind Mg antibacterial action may be associated with its release time with a possible selective bacterial killing mechanism. SEM micrographs confirmed this antibacterial ability of Mg-coated membranes after 24 h (Fig. 4B). It is important to see that clusters of bacterial cocci formed dense microcolonies in direct juxtaposition to the control surface, while the lower total of colonizing bacteria was sparsely found in Col-MgO200 and Col-MgO500 groups, which possibly related to its chemical composition. We also tested *Streptococcus aureus* biofilm and found a similar outcome (data not shown). Nanostructured MgO on Mg was found to possess antimicrobial properties against S. *aureus* in a recent study [49,79]. A separate study reported effective bactericidal effect of Mg on S *aureus* while lowering periprosthetic infection [80]. A recent review by Demishtein et al. summarized the antimicrobial properties of Mg against bacteria such as *S. epidermidis*, *P. aeruginosa*, *P. fluorescens* and *Bacillus* species and identified Mg ions at high concentration lowered adherence of the bacteria species; thus decreased biofilm formation by the same [81]; He et al. reported antimicrobial activity of MgO nanoparticles against pathogens like *Campylobacter jejuni*, *Escherichia coli* and *Salmonella enteritidis* that cause foodborne illness was due to induction of oxidative stress and membrane leakage [82].

The wettability of the samples was determined using static water drop contact angle measurement (Fig. 4C). Samples were kept in closed containers at all times in the lab environment. Immediately after ALD, both 200 and 500 cycles-coated samples were super-hydrophilic (water contact angle (WCA) ~ 0°). Between day 0 and day 14, no significant difference in water contact angle was observed on the control. However, both 200 and 500 ALD cycles coated samples became less hydrophilic (WCA ~ 50°) at day 14 despite preserving in closed containers. This shift in hydrophobicity was most likely due to the contaminants in the lab air environment. A similar shift in hydrophobicity/hydrophilicity was observed in the case of TiO_2-coated collagen membranes in a prior study [9]. Hydrophilicity is desired in antimicrobial films because the cations present in these films can interact with and disrupt the negatively charged bacterial membrane [83]. It was reported that superhydrophylic Mg-based surface significantly reduced biolfilm formation after 24 h and surface surface retained its superhydrophilic nature after long period of immersion in PBS. However, no immediate bactericidal effect associated with superhydrophilicity of the surface was observed [84].

MTS was performed to quantify the proliferation of gingival keratinocytes cultured on control and MgO-coated collagen samples [85].The cell viability is plotted in terms of absorbance value for control and collagen samples coated with 200 and 500 ALD cycles of MgO in Fig. 4D. Between day 1 and day 5, cell proliferation increased in all three samples. No significant difference in cell growth was observed between the control and the coated samples, both on day 1 and day 5 of the study. Thus, the MgO coating was not toxic to the gingival keratinocytes and did not alter the cellular growth response. Cell proliferation assay has

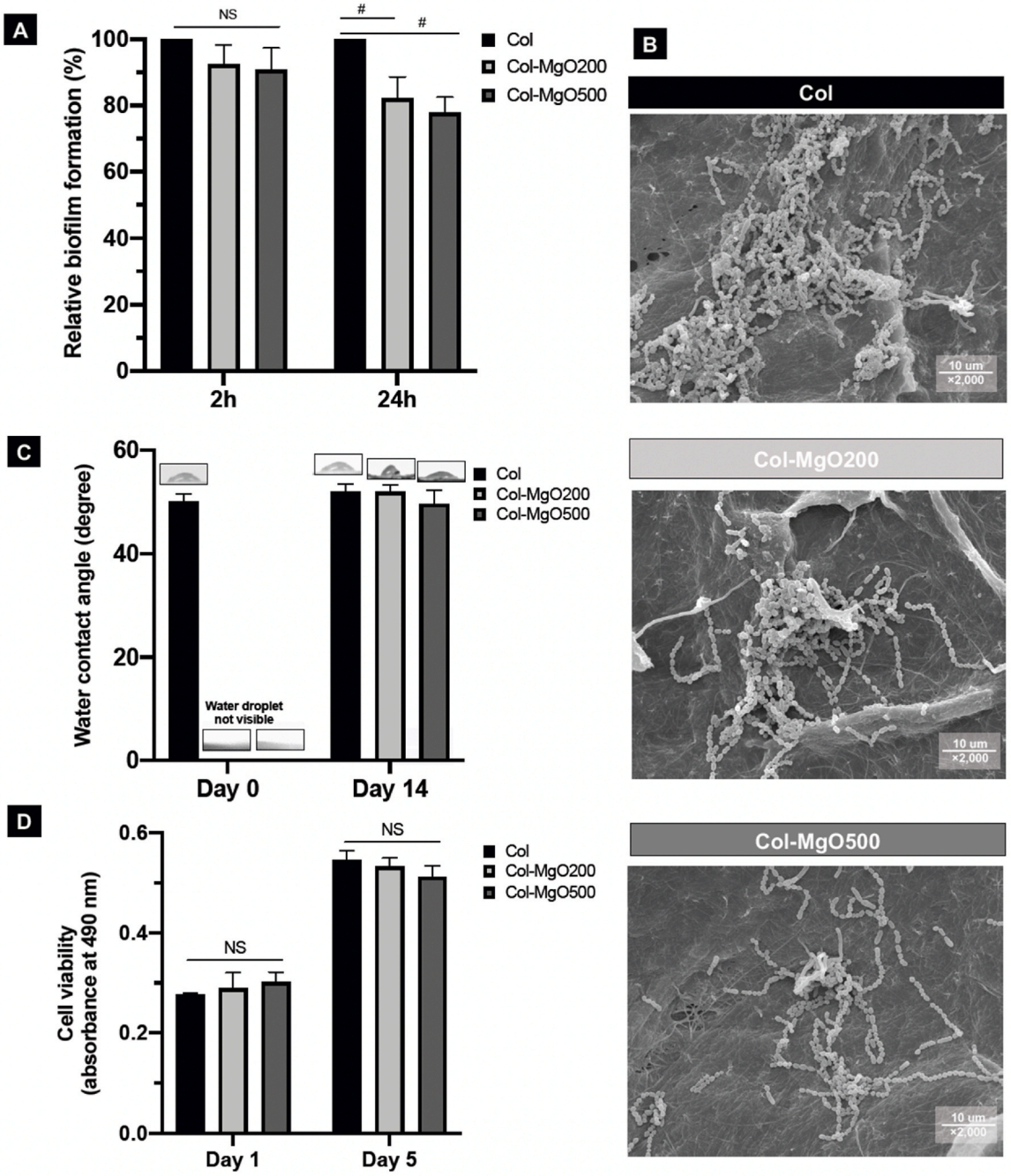

Fig. 4. *In vitro* studies performed on the control and MgO-coated collagen membranes. **A)** Antibacterial activity of Mg-coated membranes shown via a percentage of relative biofilm formation on treated membranes (200 and 500 groups) normalized from control (i.e., 100%) after polymicrobial adhesion and biofilm formation. **B)** SEM micrographs (each 10 μm scale, 2000 × magnification) of all sample groups. All analyses were performed with a one-way analysis of variance (ANOVA) followed by either Tukey's posthoc test for multiple comparisons. $^{*}p < 0.05$. **C)** WCA measurements performed using ImageJ [88] show superhydrophilicity for coated samples when analyzed immediately after ALD. **D)** MTS assay performed on control and coated samples showing non-toxicity towards gingival keratinocytes. NS = non-significant.

been used in the past with Mg-alloy based materials due to the reliable and convenient nature of the technique [74–87] over a period of time. Findings of the cell proliferation assay corroborate with the results obtained in other *in vitro* and *in vivo* studies.

3.3. In vivo studies

3.3.1. Biocompatibility analysis

Three days after subcutaneous surgery, the biocompatibility of the membranes was clearly noticed, regardless of the membranes assessed (Col, Col-MgO200, and Col-MgO500). In all histological blades, there were no foreign body reactions, in general, represented by multinucleated cells. A few amounts of inflammatory cells were observed in all groups, as represented in Fig. 5A, B, in which both tested groups (Col-MgO200 and Col-MgO500) showed higher lymphocytes count compared to Col group ($P < 0.05$), and those coated groups showed similar results (Col-MgO200=Col-MgO500; $P > 0.05$).

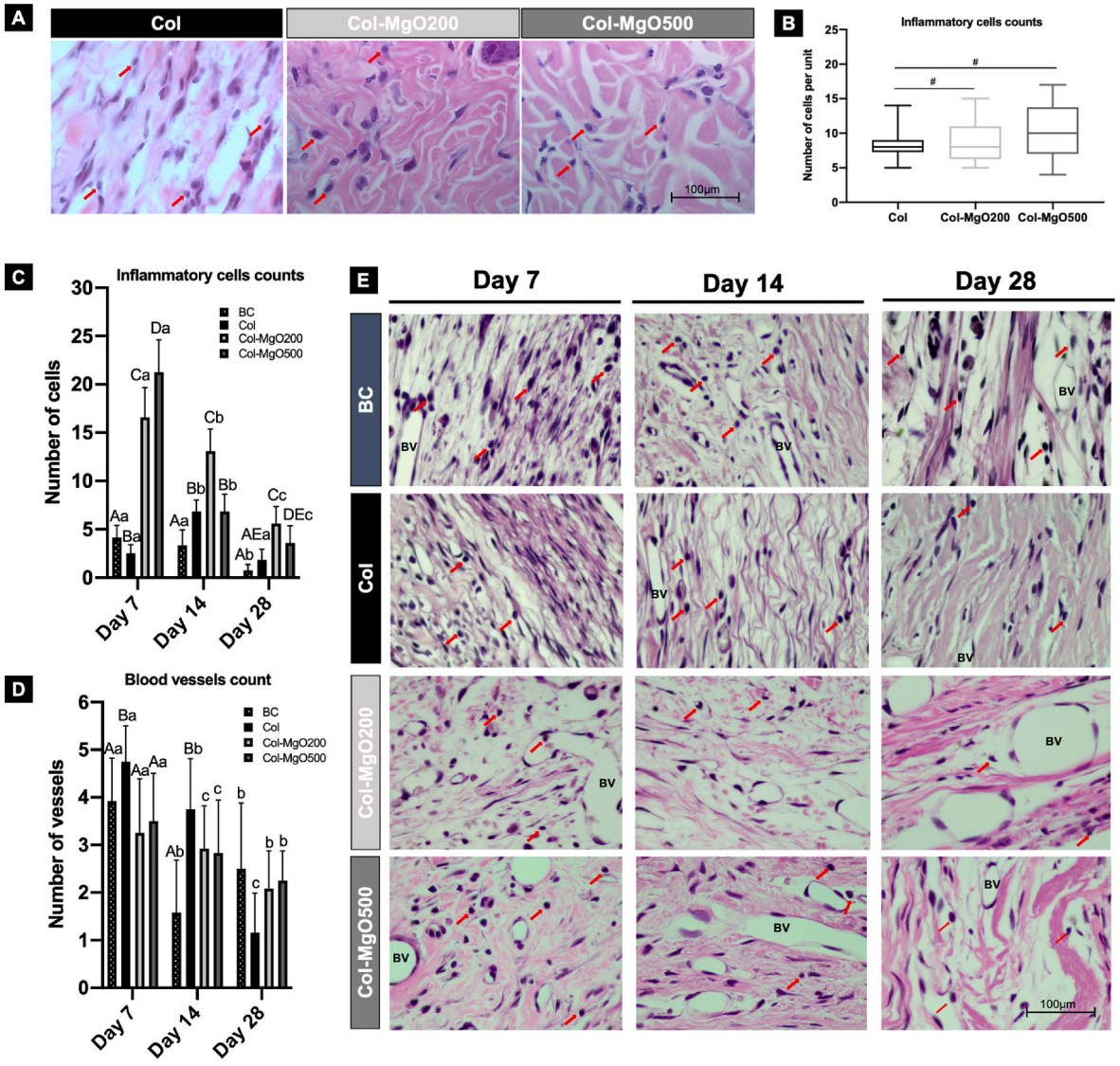

Fig. 5. Biocompatibility analysis through subcutaneous behavior surrounds the membranes (Col, Col-MgO200, and Col-MgO500) at 3 days postoperative (HE staining, Original magnification × 100). **A)** Representative images of the control and experimental groups and **B)** box plot (median representation) showed for both tested groups (Col-MgO200 and Col-MgO500) higher inflammatory cells count, with an emphasis on lymphocytes (red arrows) compared to the control group - Col (Kruskal-Wallis; $P < 0.05$). Board with **E)** Representative images and graphs of the **C)** inflammatory profile and **D)** blood vessel counts containing mean and standard deviation of BC, Col, Col-MgO200 and Col-MgO500 in the experimental periods of 7, 14 and 28 days. Different capital letters signify statistical differences between different groups within the same period. Different lowercase letters mean statistical differences of the same group in different periods ($P < 0.05$).

3.3.2. *Critical size defect assay*

3.3.2.1. Inflammatory cells and blood cells count. The representative behavior and data from inflammatory cells with emphasis on lymphocytes and the blood cell count can be seen in Fig. 5C, D. At 7 days postoperative time, the Col-MgO500 group showed the highest values, followed by Col-MgO200, BC, and Col groups ($P < 0.05$). At 14 days, Col-MgO200 cycles showed the highest number of lymphocytes ($P < 0.05$), followed by Col-MgO500 and Col (both with similar data, $P > 0.05$), and BC showed the lowest data (Fig. 5E); (Col-MgO200>Col-MgO500=Col > BC). At 28 days, the Col-MgO200 group kept on showing higher inflammatory cells compared to other groups ($P < 0.05$), while Col-MgO500, Col, and BC groups did not differ between them ($P > 0.05$).

Regarding angiogenesis, at 7 days, the Col group showed the highest values ($P < 0.05$), whereas all the other groups were similar (BC=Col-MgO200=Col-MgO500; $P > 0.05$). At 14 days, the Col group maintained the highest values compared to the others ($P < 0.05$). At 28 days, BC and Mg tested groups showed a higher number of vascular cells compared to the Col group (BC= Col-MgO200=Col-MgO500>BC; $P < 0.05$).

3.3.3. *Bone healing*

The histology characteristics of the bone healing and the behavior of the membranes during the period of analysis (7, 14, and 28 days) are shown in Fig. 6A and **B**. In a panoramic view (Fig. 6A), BC group has shown an expected behavior as a negative group, with a few newly formed bones until day 28. Col group promoted higher newly formed bone compared with BC group but clearly lower than MgO-coated groups (Col-MgO200 and Col-MgO500). MgO functionalization enhanced osteopromotive property for the collagen membrane with increased osteoblastic activity through the membranes forming higher amount of woven bone.

3.4. *Computed microtomographic (micro-CT) analysis*

The representative images of the bone defect after 28 days

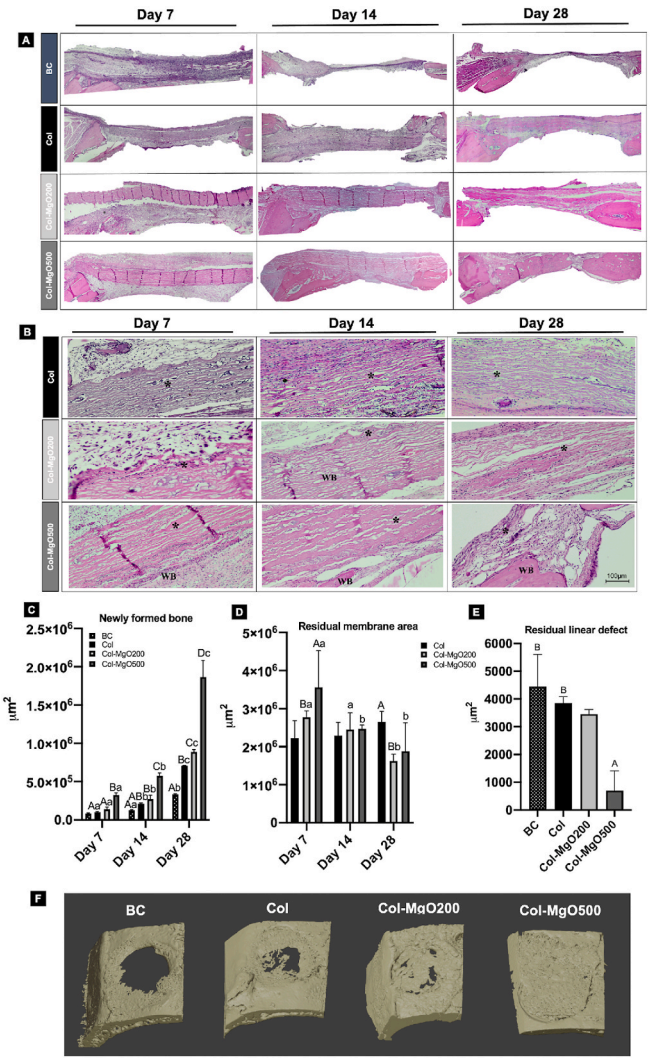

Fig. 6. *In vivo* data **(A)** Representative panoramic images of all groups (BC, Col, Col-MgO200, and Col-MgO500) in the experimental periods of 7, 14, and 28 days (Images obtained with 5 photomicrography using ×4 lens and merged in the Photoshop software; HE staining). **(B)** Representative images of the interaction between the respective membranes (*) and adjacent cells (WB: Woven Bone) at different experimental times (original magnification: x10; HE staining). Graphs showing **(C)** representative mean and standard deviation data related to newly formed bone, **(D)** residual membrane area (Two-way ANOVA test), and **(E)** residual linear defect (One-way ANOVA test). Different capital letters mean statistical differences between different groups within the same period. Different lowercase letters mean statistical differences of the same group in different periods) ($P < 0.05$). **(F)** Three-dimensional reconstruction images from scanning the calvaria defects through micro-CT for all groups: BC, Col, Col-MgO200, and Col-MgO500 at 28 days postoperatively.

postoperative are noticed in Fig. 6F. The BC group clearly showed a few amounts of hyperdensity compatible with newly formed bone, characterizing a critical-size defect. Both tested membranes (Col-MgO200 and Col-MgO500 cycles) showed a significant area of defect filling, in which the 500 cycles closed the whole defect. The control group (Col) also showed areas of defect filling; however, some hypodense regions are compatible with no bone formation.

3.5. Bone formed

At the beginning of bone healing (7 and 14 days postoperative), groups did not differ in terms of bone formation ($P > 0.05$) (Fig. 6C). From 28 days postoperative, Col-MgO500 increased the amount of bone significantly compared to all the other groups ($P < 0.05$). Collagen (Col) and Col-MgO200 showed similar data at 14 and 28 days ($P > 0.05$) (Fig. 6C).

3.6. Residual membrane area

Both MgO-coated membranes showed a level of degradation comparing the first and last period of analysis (7 and 28 days; $P > 0.05$), whereas Col kept its areas all the time ($P > 0.05$). At 28 days postoperative, Col had the highest values for residual membrane area compared to the tested membranes (Col-MgO200 and Col-MgO500; $P < 0.05$). However, both coated membranes had similar data (200 versus 500; $P > 0.05$) (Fig. 6D).

3.7. Residual linear defect

BC, Col, and Col-MgO200 cycles did not differ at the last period of analysis ($P > 0.05$); it still lacked a significant lineage to the closure of the bone defect, whereas Col-MgO500 cycles showed the lowest residual linear defect ($P < 0.05$). Several blades showed the defects almost filled with newly formed bone for Col-MgO500 (Fig. 6E).

In terms of the biological data (*in vivo* investigation), both MgO-coated membranes (Col-MgO200 and Col-MgO500) were biocompatible with the soft tissue and bone healing responses; even showing an increase in inflammation at the beginning of tissue responses and there was no foreign body reaction. None of the groups, regardless of the assessment (subcutaneous or bone defect), had phagocytic cells for all periods of analysis. The deposition of MgO with 500 cycles promoted osteopromotive action the most, which may indicate the optimum MgO concentration favorable for bone regeneration (Fig. 6B, objective 100 ×).

The MAPK/ERK and Wnt pathways are essential to the osteogenic differentiation of stem cells [89]. Mg^{2+} can selectively activate these pathways and induce stem cell differentiation. In the MAPK/ERK process, magnesium transporter 1 (MagT1), one of the major Mg^{2+} transporters, can influence the osteoinductive effect of magnesium by mediating the influx of Mg^{2+}. The internalization of Mg^{2+} improves the release of neuronal calcitonin gene-related polypeptide-a (CGRP). CGRP can bind to its receptors expressed on the surface of periosteum-derived stem cells (PSCs) and induce activation of cAMP-responsive element-binding protein 1 (CREB1) and SP7 (also known as osterix). In the Wnt process, the Mg2+ can upregulate the expression of β-catenin and its downstream genes (LEF1, DKK1), which leads to human bone marrow stromal cells(hBMSCs) to differentiate toward their osteoblast lineage. The upregulated expression of these proteins enhanced the osteogenic differentiation [38]. Mg^{2+} specific concentrations in cell cultures enhanced the mineralization of the extracellular matrix (ECM) by upregulating the expression of COL10A1 (an ECM component in healing bone) and vascular endothelial growth factor (VEGF) [39]. Further study is needed to investigate which mechanism responsible for the osteogenic effect resulted from MgO-coated collagen membranes.

Osteoblastic cells permeated the membranes maintaining their integrity, with some level of membrane degradation, causing more significant newly formed bone than the other groups. For more extensive bone reconstruction, the membranes should continue covering the reconstructed area for a more extended period, providing enough bone volume to be regenerated [89–92]. All the features described have been looked for the tissue engineering, and gathering the osteopromotive property in a resorbable membrane, such as collagen, is essential.

A few recent *in vivo* investigations [93,94] have proposed pure magnesium (99.95%) as a membrane/metal biodegradable mesh for guided bone regeneration. The creation of a bone defect in the mandibular beagle dogs was filled by a particulate bone substitute and covered by a magnesium membrane or collagen membrane (control group). Both studies showed degradation of the magnesium membranes from 8 weeks until 12 weeks allowing newly bone formed, however,

there was no significant difference in comparison with the resorbable collagen membranes available in the market. Even though the strength data was higher for the tested group, for clinical application, also thinking on the improvement of osteoblastic activity, it still necessary membrane changes. It was noticed in this study that MgO deposited by ALD on the collagen membranes maintained their integrity, covering the critical-size bone defects until the last analyzed period (on day 28), allowing almost closing of the defect with bone formed. These findings may allow more maintenance of bone reconstruction, especially in greater bone augmentation.

The most similar experimental model of this study was published by Barbeck et al. [95]. They used resorbable collagen membranes supported by a magnesium mesh with or not hydrofluoric acid-treated covering an 8 mm bone defect created on rabbit's calvaria. Regardless of group, all showed similar data, mainly related to bone formed, including tested groups compared with the collagen group without any treatment. Those data confirmed that MgO-ALD has great potential to allow the osteopromotive property on guided bone regeneration.

Magnesium as a biodegradable biomaterial has been investigated in the last decades as a metal to manufacture plates and screws for bone fixation. Its degradation allows newly formed bone with no acid product in a final release to the surrounding tissues [96,97]. *In vitro* and *in vivo* studies have shown great biocompatibility of Mg biomaterials, leading to neoangiogenesis and, consequently, osteoblastic activity [98–100]. This experimental design allowed us to assess the structural and biological features of the membranes. From the animal behavior, it was clear that 500 cycles of MgO on the membranes achieved better osteopromotive property. Col-MgO200 showed good biocompatibility and allowed newly formed bone; however, it was similar to the Col group, highlighting the need of more amount of MgO to increase bone formation as per the 500 cycles of MgO group. On the other hand, the BC group provided a few newly formed bones, which confirmed the bone defect as a critical size [101]. The osteoblastic cells going through membranes (Fig. 6), emphasizing Col-Mg500, confirmed that the functionalization had slow degradation until the end of the analysis. It allowed a significant amount of bone almost closing the defect, which is very important for the clinical application in bone reconstructions. A schematic diagram summarizing the tissue healing and antimicrobial activities of the MgO-coated samples as compared to that of the uncoated collagen is shown in Fig. 7. Among the three types of samples studied, Col-MgO500 was found to possess the best tissue healing and antimicrobial properties.

Overall, both Col-MgO200 and Col-MgO500 samples retained the morphology of the uncoated collagen membranes. SEM and TEM analyses confirmed the chemical nature of the deposited MgO film and its uniform distribution on the surface encapsulating individual fibers. Smoothness and uniformity of the film were further analyzed using AFM. ICP-MS performed on Col-MgO200 and Col-MgO500 samples showed the latter supported more sustained release of Mg^{2+} over a longer period. *In vitro* studies performed on the coated samples showed less dose-dependence and possible higher association with sustained release of Mg that enhanced the antimicrobial property of the Col-MgO500 samples. *In vivo* studies performed on the control and coated samples further corroborate the findings of the characterization and *in vitro* studies deeming the Col-MgO500 samples best candidate among the tested groups over a longer period (28 days) in terms of the inflammatory response in the host body. The number of vascular cells for Col-MgO500 was also higher and none of the samples had any foreign

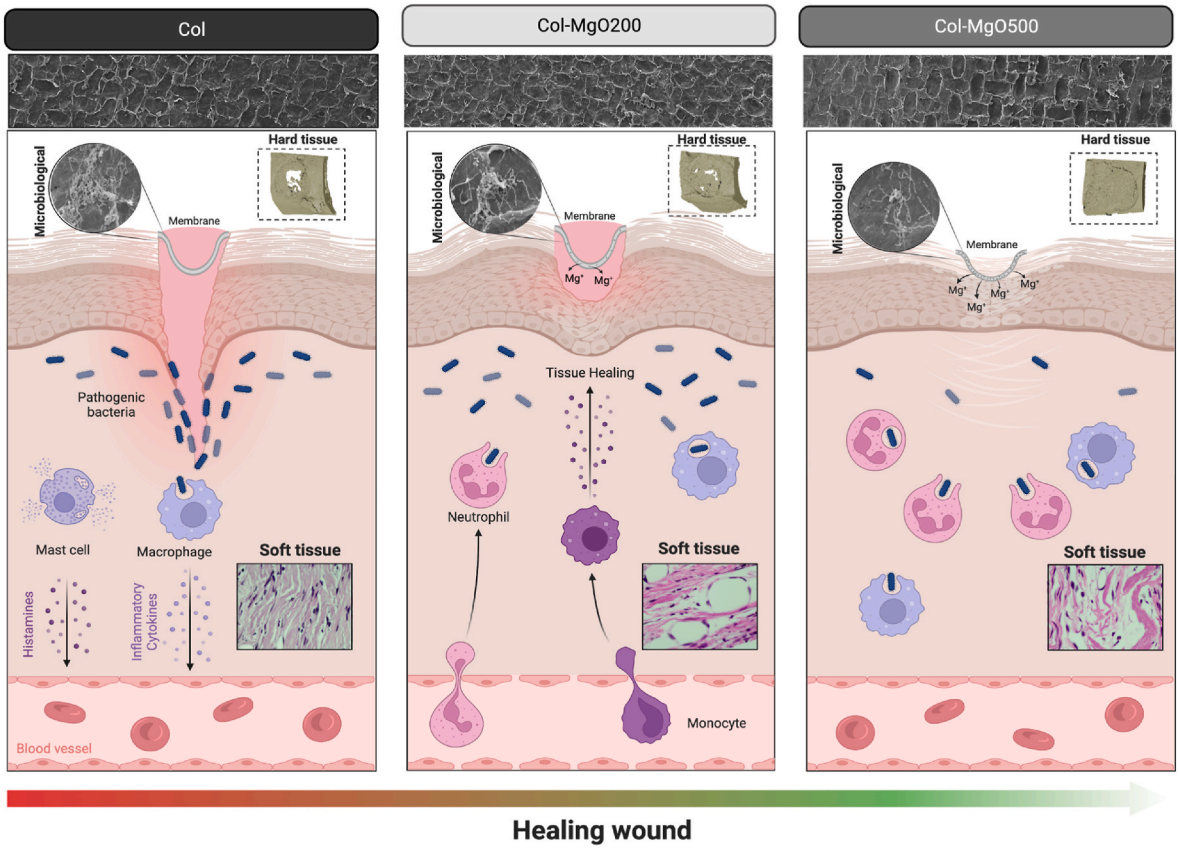

Fig. 7. Summary of *in vitro* and *in vivo* studies performed on Col, Col-MgO200 and Col-MgO500 samples. The schematic diagram shows how MgO-coated collagen samples promote tissue healing while preventing antimicrobial infections at the same time. Mg has antibacterial properties attributed to a large amount of OH^- produced during degradation, creating an alkaline environment. Mg ions also stimulate osteopromotive by activating signal transduction pathways such as the MAPK/ERK and Wnt and increased vascularized bone repairs by promoting neovascularization.

body reaction [102–104]. In addition, bone healing was improved, and higher number of newly formed bones was observed for Col-MgO500 after 28 days. The Col-MgO500 samples indeed possessed higher antimicrobial and osteopromotive properties. To the best of our knowledge, this study was the first one to assess those parameters. Thus, the functionalization with MgO of collagen membranes, especially using 500 cycles of MgO, showed promising data for biomedical applications.

Based on the improvement of the mechanical and biological properties developed by the col-500 membrane, its clinical application can be an important alternative to overcome the difficulties of conventional collagen membranes, which are widely used, maintaining good permeability for osteoblastic cells and blood vessels, and the three-dimensional volume of the place where it is applied [105,106]. Future craniomaxillofacial and orthopedic clinical investigations should be designed to assess those biological features for market production.

3.8. Limitations

One of the most common disadvantages of ALD is that it can be a slow process. It took a little over 4 h to perform 200 cycles of ALD and deposit 24 nm of MgO based on the recipe used for this study. However, the processes used in this study focused on room temperature thermal ALD which can be sped up by using many developed and current developing techniques such as plasma enhanced ALD (PEALD) [107], Spatial ALD [108] among others.

As an *in vitro* and *in vivo* (animal model) study, there is a limitation regarding the translation to clinical behavior. The rats Wistar used here and other rodents, although they have their metabolism at least three to four times faster than humans, there is approximately 95% of similarity in the genes [109,110]. The faster metabolism of these animals (3–4 times) allows us to compare the biological behavior of the membranes in the long term. 1 month postoperatively corresponds to 3–4 months in clinical speculation, which is more than enough for the analysis of the time of degradation of the membranes and osteopromotive potential for bone reconstructions.

In addition, despite simulating the interaction of the biomaterial in a living organism, animal experimentation is carried out in a controlled environment, with controlled diet and temperature, in accordance with permitted ethical standards, unlike what occurs in the human organism, exposed to different conditions, such as several simultaneous systemic diseases. It is important to point out that rodents have great resistance when subjected to adverse situations to the homeostatic, such as what is done in the research [109,110]. Therefore, a pre-clinical assessment is essential to confirm the membrane's compatibility and enhancement of bone healing before a human investigation.

4. Conclusion

Successful room-temperature ALD of MgO thin films enabled the use of temperature-sensitive material collagen as the substrate. ALD being a conformal technique, is able to coat the individual collagen fibers uniformly. The nature of the film was determined to be amorphous and free from any impurities. The coated collagen membrane allowed the controlled release of Mg ions, was non-toxic to human cells, and showed good antimicrobial activity against bacterial biofilm. Both tested functionalized membranes (Col-Mg200 and 500) showed good compatibility in the subcutaneous tissue, and 500 cycles of MgO on collagen membranes achieved great osteopromotive potential on critical-size bone defects in the calvaria rats model.

CRediT authorship contribution statement

Soumya Saha: Conceptualization, Methodology, Validation, Investigation, Writing – original draft. **Raphael Cavalcante Costa:** Conceptualization, Methodology, Validation, Investigation. **Mirela Caroline Silva:** Conceptualization, Methodology, Validation, Investigation. **João Matheus Fonseca-Santos:** Conceptualization, Methodology, Validation, Investigation. **Lin Chen:** Conceptualization, Methodology, Validation, Investigation. **Abhijit H. Phakatkar:** Conceptualization, Methodology, Validation, Investigation. **Harshdeep Bhatia:** Conceptualization, Methodology, Validation, Investigation. **Leonardo P. Faverani:** Methodology, Validation, Writing – review & editing, Supervision. **Valentim A.R. Barão:** Methodology, Validation, Writing – review & editing, Supervision. **Tolou Shokuhfar:** Methodology, Validation, Writing – review & editing, Supervision. **Cortino Sukotjo:** Methodology, Validation, Writing – review & editing, Supervision. **Christos Takoudis:** Methodology, Validation, Writing – review & editing, Supervision.

Declaration of competing interest

The authors declare that they have no competing financial interests or personal relationships that could have appeared to influence the work reported in this manuscript.

Acknowledgements

This work has been partially carried out through funding by Coordenação de Aperfeiçoamento de Pessoal de Nível Superior - Brazil (CAPES), in the scope of Programa Capes-PrInt - Funding code: 001″ Process: 88887.194785/2018-00, and the Conselho Nacional de Desenvolvimento Cientifico e Tecnologico (CNPq, Brazil) (#309970/2022-9) to L.P.F. V.A.R.B. received support from CNPq (Brazil) (#307471/2021-7) and São Paulo Research Foundation (FAPESP, Brazil) (#2020/05231-4 and 2022/16267-5). R.C.C. received support from FAPESP (Brazil) (#2020/10436-4). Partial funding from the UIC College of Dentistry (C. S.) and the National Science Foundation, grant number DMR-1309114. (C.T.) is also greatly appreciated. AFM scans were performed by Sungjoon Kim, graduate student, Dr. Berry's lab, University of Illinois Chicago. The authors are thankful to the staff scientists at University of Illinois Urbana-Champaign, Dr. Ashley Blystone and Dr. Jessica Spear from Microanalysis facility and Materials Research Laboratory respectively for assisting with the ICP-MS and SEM characterizations.

Appendix A. Supplementary data

Supplementary data to this article can be found online at https://doi.org/10.1016/j.bioactmat.2023.07.013.

References

[1] Bone-grafting materials: their uses, advantages and disadvantages, J. Am. Dent. Assoc. 133 (2002) 1125–1126, https://doi.org/10.14219/JADA.ARCHIVE.2002.0341.
[2] T.W. Bauer, G.F. Muschler, Bone graft materials, clinical orthopaedics and related research number, 371 (n.d.) 10–27, http://journals.lww.com/clinorthop. (Accessed 6 May 2022).
[3] G. Tomoaia, R.D. Pasca, On the collagen mineralization. A review, Med. Pharm. Rep. 88 (2015) 15–22, https://doi.org/10.15386/CJMED-359.
[4] H. Madry, Tissue-engineered cartilage products, Principles Tissue Eng. (2020) 1499–1509, https://doi.org/10.1016/B978-0-12-818422-6.00082-4.
[5] X. Liang, A.D. Lynn, D.M. King, S.J. Bryant, A.W. Weimer, Biocompatible interface films deposited within porous polymers by atomic layer deposition (ALD), ACS Appl. Mater. Interfaces 1 (2009) 1988–1995, https://doi.org/10.1021/AM9003667/ASSET/IMAGES/LARGE/AM-2009-003667_0009.JPEG.
[6] W. Wagermaier, P. Fratzl, Collagen, Poly. Sci.: A Comprehensive Reference 10 (2012) 35–55, https://doi.org/10.1016/B978-0-444-53349-4.00247-8, 9.
[7] D.A. Wahl, J.T. Czernuszka, Collagen-hydroxyapatite composites for hard tissue repair, Eur. Cell. Mater. 11 (2006) 43–56, https://doi.org/10.22203/ECM.V011A06.
[8] B. Marelli, C.E. Ghezzi, J.E. Barralet, A.R. Boccaccini, S.N. Nazhat, Three-dimensional mineralization of dense nanofibrillar collagen-bioglass hybrid scaffolds, Biomacromolecules 11 (2010) 1470–1479, https://doi.org/10.1021/BM1001087/SUPPL_FILE/BM1001087_SI_001.PDF.
[9] A.K. Bishal, C. Sukotjo, J.R. Jokisaari, R.F. Klie, C.G. Takoudis, Enhanced bioactivity of collagen fiber functionalized with room temperature atomic layer deposited titania, ACS Appl. Mater. Interfaces 10 (2018) 34443–34454, https://

doi.org/10.1021/ACSAMI.8B05857/ASSET/IMAGES/LARGE/AM-2018-05857U_0007.JPEG.
[10] I. Kanayama, H. Miyaji, H. Takita, E. Nishida, M. Tsuji, B. Fugetsu, L. Sun, K. Inoue, A. Ibara, T. Akasaka, T. Sugaya, M. Kawanami, Comparative study of bioactivity of collagen scaffolds coated with graphene oxide and reduced graphene oxide, Int. J. Nanomed. 9 (2014) 3363–3373, https://doi.org/10.2147/IJN.S62342.
[11] R.W. Johnson, A. Hultqvist, S.F. Bent, A brief review of atomic layer deposition: from fundamentals to applications, Mater. Today 17 (2014) 236–246, https://doi.org/10.1016/J.MATTOD.2014.04.026.
[12] J. Hornak, Synthesis, properties and selected technical applications of magnesium oxide nanoparticles: a review, Int. J. Mol. Sci. 22 (2021), 12752, https://doi.org/10.3390/ijms222312752.
[13] T. Lopez, I. Garcia-Cruz, R. Gomez, Synthesis of magnesium oxide by the sol-gel method: effect of the pH on the surface hydroxylation, J. Catal. 127 (1991) 75–85.
[14] M.S. Idris, S. Shanmugan, Evaluation of the thermal performance of high-power LED using magnesium oxide thin film as heat spreader, Mater. Chem. Phys. 277 (2022), 125588, https://doi.org/10.1016/j.matchemphys.2021.125588.
[15] D. Gaur, S. Sharma, A. Sharma, D.K. Sharma, S. Shukla, Structural, electronic structure, and photovoltaic studies of MgO/TiO2/ITO heterostructures, J. Electron. Mater. 51 (2022) 314–320, https://doi.org/10.1007/S11664-021-09290-Z/TABLES/1.
[16] M.R.A. Cruz, E. Luévano-Hipólito, R. Garza-Hernández, L.M. Torres-Martínez, MgO and Mg(OH)2 thin films prepared by the SILAR method and their CO2 photocatalytic performance, J. Mater. Sci. 57 (2022) 18739–18753, https://doi.org/10.1007/S10853-022-07837-X/FIGURES/12.
[17] V. Hass, H. Liu, W. Cook, M.P. Walker, Y. Wang, Distinct effects of polyphenols and solvents on dentin collagen crosslinking interactions and biostability, Dent. Mater. 37 (2021) 1794, https://doi.org/10.1016/J.DENTAL.2021.09.009.
[18] K. Lewandowska, M. Szulc, A. Sionkowska, Effect of solvent on the hydrodynamic properties of collagen, Polym 13 (2021) 3626, https://doi.org/10.3390/POLYM13213626, 13 (2021) 3626.
[19] R. Salsas-Escat, C.M. Stultz, The molecular mechanics of collagen degradation: implications for human disease, Exp. Mech. 49 (2009) 65–77, https://doi.org/10.1007/S11340-007-9105-1/TABLES/1.
[20] S. Hashemi Astaneh, L.P. Faverani, C. Sukotjo, C.G. Takoudis, Atomic layer deposition on dental materials: processing conditions and surface functionalization to improve physical, chemical, and clinical properties - a review, Acta Biomater. 121 (2021) 103–118, https://doi.org/10.1016/J.ACTBIO.2020.11.024.
[21] P.N. Arendt, S.R. Foltyn, Biaxially textured IBAD-MgO templates for YBCO-coated conductors, n.d, www.mrs.org/publications/bulletin. (Accessed 15 June 2023).
[22] C.P. Wang, K.B. Do, M.R. Beasley, T.H. Geballe, R.H. Hammond, Deposition of in-plane textured MgO on amorphous Si3N4 substrates by ion-beam-assisted deposition and comparisons with ion-beam-assisted deposited yttria-stabilized-zirconia, Appl. Phys. Lett. 71 (1997) 2955–2957, https://doi.org/10.1063/1.120227.
[23] O.P. Das, S.K. Pandey, Systematic evolution of optical bandgap and local chemical state in transparent MgO and HfO2 resistive switching materials, Phys. Status Solidi Basic Res. 259 (2022), 2200103, https://doi.org/10.1002/pssb.202200103.
[24] P.J.W. Moll, Focused Ion Beam Microstructuring of Quantum Matter, Https://Doi.Org/10.1146/Annurev-Conmatphys-033117-054021. 9 (2018) 147–162. https://doi.org/10.1146/ANNUREV-CONMATPHYS-033117-054021.
[25] S. Lo, M.B. Fauzi, Current update of collagen nanomaterials—fabrication, characterisation and its applications: a review, Pharmaceutics 13 (2021) 1–18, https://doi.org/10.3390/PHARMACEUTICS13030316.
[26] T. Jurca, M.J. Moody, A. Henning, J.D. Emery, B. Wang, J.M. Tan, T.L. Lohr, L. J. Lauhon, T.J. Marks, Low-temperature atomic layer deposition of MoS2 films, Angew. Chem. Int. Ed. 56 (2017) 4991–4995, https://doi.org/10.1002/ANIE.201611838.
[27] M. Putkonen, P. Sippola, L. Svärd, T. Sajavaara, J. Vartiainen, I. Buchanan, U. Forsström, P. Simell, T. Tammelin, Low-temperature atomic layer deposition of SiO2/Al2O3 multilayer structures constructed on self-standing films of cellulose nanofibrils, Phil. Trans. Math. Phys. Eng. Sci. (2018) 376, https://doi.org/10.1098/RSTA.2017.0037.
[28] M.D. Groner, F.H. Fabreguette, J.W. Elam, S.M. George, Low-temperature Al2O3 atomic layer deposition, Chem. Mater. 16 (2004) 639–645, https://doi.org/10.1021/CM0304546/ASSET/IMAGES/LARGE/CM0304546F00012.JPEG.
[29] M.Z. Ansari, D.K. Nandi, P. Janicek, S.A. Ansari, R. Ramesh, T. Cheon, B. Shong, S.H. Kim, Low-temperature atomic layer deposition of highly conformal tin nitride thin films for energy storage Devices, ACS Appl. Mater. Interfaces 11 (2019) 43608–43621, https://doi.org/10.1021/ACSAMI.9B15790/ASSET/IMAGES/LARGE/AM9B15790_0010.JPEG.
[30] A.K. Bishal, C. Sukotjo, C.G. Takoudis, Room temperature TiO2 atomic layer deposition on collagen membrane from a titanium alkylamide precursor, J. Vac. Sci. Technol. A: Vacuum, Surfaces, and Films 35 (2016), 01B134, https://doi.org/10.1116/1.4972245.
[31] P.K. Rout, S. Roy, S. Ganguly, D.K. Rathore, A Review on Properties of Magnesium-Based Alloys for Biomedical Applications, Biomed Phys Eng Express, 2022, https://doi.org/10.1088/2057-1976/AC6D81.
[32] A. Hoppe, N.S. Güldal, A.R. Boccaccini, A review of the biological response to ionic dissolution products from bioactive glasses and glass-ceramics, Biomaterials 32 (2011) 2757–2774, https://doi.org/10.1016/J.BIOMATERIALS.2011.01.004.
[33] G. Song, Control of biodegradation of biocompatable magnesium alloys, Corrosion Sci. 49 (2007) 1696–1701, https://doi.org/10.1016/J.CORSCI.2007.01.001.
[34] E. Landi, G. Logroscino, L. Proietti, A. Tampieri, M. Sandri, S. Sprio, Biomimetic Mg-substituted hydroxyapatite: from synthesis to in vivo behaviour, J. Mater. Sci. Mater. Med. 19 (2008) 239–247, https://doi.org/10.1007/S10856-006-0032-Y.
[35] X. Zhang, P. Huang, G. Jiang, M. Zhang, F. Yu, X. Dong, L. Wang, Y. Chen, W. Zhang, Y. Qi, W. Li, H. Zeng, A novel magnesium ion-incorporating dual-crosslinked hydrogel to improve bone scaffold-mediated osteogenesis and angiogenesis, Mater. Sci. Eng. C 121 (2021), 111868, https://doi.org/10.1016/j.msec.2021.111868.
[36] Y. Kang, C. Xu, L. Meng, X. Dong, M. Qi, D. Jiang, Exosome-functionalized magnesium-organic framework-based scaffolds with osteogenic, angiogenic and anti-inflammatory properties for accelerated bone regeneration, Bioact. Mater. 18 (2022) 26–41, https://doi.org/10.1016/j.bioactmat.2022.02.012.
[37] A. Chaya, S. Yoshizawa, K. Verdelis, N. Myers, B.J. Costello, D.T. Chou, S. Pal, S. Maiti, P.N. Kumta, C. Sfeir, In vivo study of magnesium plate and screw degradation and bone fracture healing, Acta Biomater. 18 (2015) 262–269, https://doi.org/10.1016/j.actbio.2015.02.010.
[38] Y. Zhang, J. Xu, Y.C. Ruan, M.K. Yu, M. O'Laughlin, H. Wise, D. Chen, L. Tian, D. Shi, J. Wang, S. Chen, J.Q. Feng, D.H.K. Chow, X. Xie, L. Zheng, L. Huang, S. Huang, K. Leung, N. Lu, L. Zhao, H. Li, D. Zhao, X. Guo, K. Chan, F. Witte, H. C. Chan, Y. Zheng, L. Qin, Implant-derived magnesium induces local neuronal production of CGRP to improve bone-fracture healing in rats, Nat. Med. 22 (2016) 1160–1169, https://doi.org/10.1038/nm.4162.
[39] S. Yoshizawa, A. Brown, A. Barchowsky, C. Sfeir, Role of magnesium ions on osteogenic response in bone marrow stromal cells, in: Connect. Tissue Res., Taylor & Francis, 2014, pp. 155–159, https://doi.org/10.3109/03008207.2014.923877.
[40] N. Sezer, Z. Evis, S.M. Kayhan, A. Tahmasebifar, M. Koç, Review of magnesium-based biomaterials and their applications, J. Magnesium Alloys 6 (2018) 23–43, https://doi.org/10.1016/J.JMA.2018.02.003.
[41] S. Dutta, K.B. Devi, S. Gupta, B. Kundu, V.K. Balla, M. Roy, Mechanical and in vitro degradation behavior of magnesium-bioactive glass composites prepared by SPS for biomedical applications, J. Biomed. Mater. Res. B Appl. Biomater. 107 (2019) 352–365, https://doi.org/10.1002/JBM.B.34127.
[42] M. Rahmati, S. Stötzel, T. el Khassawna, K. Iskhahova, D.C. Florian Wieland, B. Zeller Plumhoff, H.J. Haugen, Early Osteoimmunomodulatory Effects of Magnesium–Calcium–Zinc Alloys, vol. 12, 2021, https://doi.org/10.1177/20417314211047100.
[43] S. Saha, W. Lestari, C. Dini, M.N. Sarian, H. Hermawan, V.A.R. Barão, C. Sukotjo, C. Takoudis, Corrosion in Mg-alloy biomedical implants- the strategies to reduce the impact of the corrosion inflammatory reaction and microbial activity, J. Magnesium Alloys 10 (2022) 3306–3326, https://doi.org/10.1016/J.JMA.2022.10.025.
[44] S. Vangelista, R. Mantovan, A. Lamperti, G. Tallarida, B. Kutrzeba-Kotowska, S. Spiga, M. Fanciulli, Low-temperature atomic layer deposition of MgO thin films on Si, J. Phys. D Appl. Phys. 46 (2013), 485304, https://doi.org/10.1088/0022-3727/46/48/485304.
[45] B.B. Burton, D.N. Goldstein, S.M. George, Atomic layer deposition of MgO using bis(ethylcyclopentadienyl)magnesium and H2O, J. Phys. Chem. C 113 (2009) 1939–1946, https://doi.org/10.1021/JP806088M/ASSET/IMAGES/JP-2008-06088M_M009.GIF.
[46] H.J. Svec, D.S. Gibbs, Kinetics of the reaction between magnesium and water vapour, J. Electrochem. Soc. 104 (1957) 434–438. http://link.aip.org/link/JESOAN/v104/i7/p434/s1&Agg=doi.
[47] P.H. Stauffer, K.C.L. Joshua, B.J. Travis, P. Lichtner, G. Zyvoloski, Joule – thomson effects on the flow of liquid water, Transport Porous Media 105 (2014) 471–485, https://doi.org/10.1007/s11242-014-0379-3.
[48] M. Shahmohammadi, E. Pensa, H. Bhatia, B. Yang, G. Jursich, C.G. Takoudis, Enhancing the surface properties and functionalization of polymethyl methacrylate with atomic layer-deposited titanium(IV) oxide, J. Mater. Sci. 55 (2020) 17151–17169, https://doi.org/10.1007/s10853-020-05274-2.
[49] S. Hayat, S. Muzammil, M.H. Rasool, Z. Nisar, S.Z. Hussain, A.N. Sabri, S. Jamil, In vitro antibiofilm and anti-adhesion effects of magnesium oxide nanoparticles against antibiotic resistant bacteria, Microbiol. Immunol. 62 (2018) 211–220, https://doi.org/10.1111/1348-0421.12580.
[50] C. Takoudis, M. Singh, S. Selvaraj, Multi-metal films, alternating film multilayers, formation methods and deposition system, Patent US-1 21 (2019) 4817, issued in February.
[51] A.K. Bishal, C. Sukotjo, C.G. Takoudis, Room temperature TiO2 atomic layer deposition on collagen membrane from a titanium alkylamide precursor, J. Vac. Sci. Technol. A: Vacuum, Surfaces, and Films 35 (2016), 01B134, https://doi.org/10.1116/1.4972245.
[52] D. Nečas, P. Klapetek, Gwyddion: an open-source software for SPM data analysis, Cent. Eur. J. Phys. 10 (2012) 181–188, https://doi.org/10.2478/S11534-011-0096-2.
[53] J. Walton, P. Wincott, N. Fairley, A. Carrick, Peak Fitting with CasaXPS: A Casa Pocket Book, Accolyte Science, 2010. https://www.research.manchester.ac.uk/portal/en/publications/peak-fitting-with-casaxps(1710f697-022a-4fff-878f-2ea679a8996c).html. (Accessed 26 November 2021).
[54] R.C. Costa, J.G.S. Souza, M. Bertolini, B. Retamal-Valdes, M. Feres, V.A.R. Barão, Extracellular biofilm matrix leads to microbial dysbiosis and reduces biofilm susceptibility to antimicrobials on titanium biomaterial: an in vitro and in situ study, Clin. Oral Implants Res. 31 (2020) 1173–1186, https://doi.org/10.1111/CLR.13663.

[55] J.G.S. Souza, M. Bertolini, R.C. Costa, J.M. Cordeiro, B.E. Nagay, A.B. de Almeida, B. Retamal-Valdes, F.H. Nociti, M. Feres, E.C. Rangel, V.A.R. Barão, Targeting pathogenic biofilms: newly developed superhydrophobic coating favors a host-compatible microbial profile on the titanium surface, ACS Appl. Mater. Interfaces 12 (2020) 10118–10129, https://doi.org/10.1021/ACSAMI.9B22741/ASSET/IMAGES/LARGE/AM9B22741_0006.JPEG.

[56] R.C. Costa, J.G.S. Souza, J.M. Cordeiro, M. Bertolini, E.D. de Avila, R. Landers, E. C. Rangel, C.A. Fortulan, B. Retamal-Valdes, N.C. da Cruz, M. Feres, V.A.R. Barão, Synthesis of bioactive glass-based coating by plasma electrolytic oxidation: untangling a new deposition pathway toward titanium implant surfaces, J. Colloid Interface Sci. 579 (2020) 680–698, https://doi.org/10.1016/J.JCIS.2020.06.102.

[57] M. Jaeggi, S. Gyr, M. Astasov-Frauenhoffer, N.U. Zitzmann, J. Fischer, N. Rohr, Influence of different zirconia surface treatments on biofilm formation in vitro and in situ, Clin. Oral Implants Res. 33 (2022) 424–432, https://doi.org/10.1111/CLR.13902.

[58] M. Bertolini, R. Vazquez Munoz, L. Archambault, S. Shah, J.G.S. Souza, R. C. Costa, A. Thompson, Y. Zhou, T. Sobue, A. Dongari-Bagtzoglou, Mucosal bacteria modulate Candida albicans virulence in oropharyngeal candidiasis, mBio 12 (2021), https://doi.org/10.1128/MBIO.01937-21.

[59] N.P. du Sert, V. Hurst, A. Ahluwalia, S. Alam, M.T. Avey, M. Baker, W.J. Browne, A. Clark, I.C. Cuthill, U. Dirnagl, M. Emerson, P. Garner, S.T. Holgate, D. W. Howells, N.A. Karp, S.E. Lazic, K. Lidster, C.J. MacCallum, M. Macleod, E. J. Pearl, O.H. Petersen, F. Rawle, P. Reynolds, K. Rooney, E.S. Sena, S. D. Silberberg, T. Steckler, H. Würbel, The ARRIVE guidelines 2.0: updated guidelines for reporting animal research, PLoS Biol. 18 (2020), e3000410, https://doi.org/10.1371/JOURNAL.PBIO.3000410.

[60] S. Ardizzone, C.L. Bianchi, M. Fadoni, B. Vercelli, Magnesium salts and oxide: an XPS overview, Appl. Surf. Sci. 119 (1997) 253–259, https://doi.org/10.1016/S0169-4332(97)00180-3.

[61] J.T. Newberg, D.E. Starr, S. Yamamoto, S. Kaya, T. Kendelewicz, E.R. Mysak, S. Porsgaard, M.B. Salmeron, G.E. Brown, A. Nilsson, H. Bluhm, Formation of hydroxyl and water layers on MgO films studied with ambient pressure XPS, Surf. Sci. 605 (2011) 89–94, https://doi.org/10.1016/J.SUSC.2010.10.004.

[62] T. Athar, A. Hakeem, W. Ahmed, Synthesis of MgO nanopowder via non aqueous sol-gel method, Adv. Sci. Lett. 7 (2012) 27–29, https://doi.org/10.1166/ASL.2012.2190.

[63] P. Raz, T. Brosh, G. Ronen, H. Tal, Tensile properties of three selected collagen membranes, BioMed Res. Int. 2019 (2019), https://doi.org/10.1155/2019/5163603.

[64] S. Li, H. Chen, N. Lee, R. Ringshia, D. Yuen, A Comparative Study of Zimmer BioMend ® and BioMend ® Extend TM Membranes Made at Two Different Manufacturing Facilities, 2013.

[65] F. Liu, K. Zhu, Y. Ma, Z. Yu, B.-S. Chiou, M. Jia, M. Chen, F. Zhong, Collagen films with improved wet state mechanical properties by mineralization, Food Hydrocolloids 139 (2023), 108579, https://doi.org/10.1016/J.FOODHYD.2023.108579.

[66] J.G. López-Santiago, P.A. Sundaram, Mechanical properties of mineralized collagen type I rat-tail tendon fascicles, Eur. J. Dent. Oral Heal. 3 (2022) 7–11, https://doi.org/10.24018/EJDENT.2022.3.4.160.

[67] T. Qiang, L. Chen, Z. Yan, X. Liu, Evaluation of a novel collagenous matrix membrane cross-linked with catechins catalyzed by laccase: a sustainable biomass, J. Agric. Food Chem. 67 (2019) 1504–1512, https://doi.org/10.1021/acs.jafc.8b05810.

[68] W. Kangjian, D. Nianhua, X. Shiwei, Y. Yichun, D. Weihua, Preparation and characterization of collagen-chitosan-chondroitin sulfate composite membranes, J. Membr. Biol. 245 (2012) 707–716, https://doi.org/10.1007/S00232-012-9442-6.

[69] M. Lashkari, M. Rahmani, Y. Yousefpoor, M. Ahmadi-Zeidabadi, R. Faridi-Majidi, Z. Ameri, M. Salary, S. Azizi, A. Shahabi, A. Rahi, M.J. Mirzaei-Parsa, Cell-based wound dressing: bilayered PCL/gelatin nanofibers-alginate/collagen hydrogel scaffold loaded with mesenchymal stem cells, Int. J. Biol. Macromol. 239 (2023), 124099, https://doi.org/10.1016/j.ijbiomac.2023.124099.

[70] S. Choy, D. Van Lam, S.M. Lee, D.S. Hwang, Prolonged biodegradation and improved mechanical stability of collagen via vapor-phase Ti stitching for long-term tissue regeneration, ACS Appl. Mater. Interfaces 11 (2019) 38440–38447, https://doi.org/10.1021/ACSAMI.9B12196.

[71] S.M. Lee, E. Pippel, U. Gösele, C. Dresbach, Y. Qin, C.V. Chandran, T. Bräuniger, G. Hause, M. Knez, Greatly increased toughness of infiltrated spider silk, Science 324 (2009) 488–492, https://doi.org/10.1126/science.1168162.

[72] S.M. Lee, G. Grass, G.M. Kim, C. Dresbach, L. Zhang, U. Gösele, M. Knez, Low-temperature ZnO atomic layer deposition on biotemplates: flexible photocatalytic ZnO structures from eggshell membranes, Phys. Chem. Chem. Phys. 11 (2009) 3608–3614, https://doi.org/10.1039/b820436e.

[73] S.M. Lee, E. Pippel, M. Knez, Metal infiltration into biomaterials by ALD and CVD: a comparative study, ChemPhysChem 12 (2011) 791–798, https://doi.org/10.1002/cphc.201000923.

[74] F. Barrère, C.A. van Blitterswijk, K. de Groot, Bone regeneration: molecular and cellular interactions with calcium phosphate ceramics, Int. J. Nanomed. 1 (2006) 317. /pmc/articles/PMC2426803/. (Accessed 29 May 2022).

[75] J. Liu, H. Zeng, P. Xiao, A. Yang, X. Situ, Y. Wang, X. Zhang, W. Li, W. Pan, Y. Wang, Sustained release of magnesium ions mediated by a dynamic mechanical hydrogel to enhance BMSC proliferation and differentiation, ACS Omega 5 (2020) 24477–24486, https://doi.org/10.1021/ACSOMEGA.0C02946/ASSET/IMAGES/LARGE/AO0C02946_0006.JPEG.

[76] W. Wu, X. Yu, Y. Zhao, X. Jiang, H. Yang, Characterization and biocompatibility of insoluble corrosion products of AZ91 Mg alloys, ACS Omega 4 (2019), 15139, https://doi.org/10.1021/ACSOMEGA.9B02041.

[77] S.V.S. Prasad, S.B. Prasad, K. Verma, R.K. Mishra, V. Kumar, S. Singh, The role and significance of Magnesium in modern day research-A review, J. Magnesium Alloys 10 (2022) 1–61, https://doi.org/10.1016/J.JMA.2021.05.012.

[78] J.G. Jung, S.H. Park, H. Yu, Y.M. Kim, Y.K. Lee, B.S. You, Improved mechanical properties of Mg–7.6Al–0.4Zn alloy through aging prior to extrusion, Scripta Mater. 93 (2014) 8–11, https://doi.org/10.1016/J.SCRIPTAMAT.2014.08.017.

[79] J. Lin, N.Y.T. Nguyen, C. Zhang, A. Ha, H.H. Liu, Antimicrobial properties of MgO nanostructures on magnesium substrates, ACS Omega 5 (2020) 24613–24627, https://doi.org/10.1021/ACSOMEGA.0C03151/SUPPL_FILE/AO0C03151_LIVESLIDES.MP4.

[80] Y. Li, G. Liu, Z. Zhai, L. Liu, H. Li, K. Yang, L. Tan, P. Wan, X. Liu, Z. Ouyang, Z. Yu, T. Tang, Z. Zhu, X. Qu, K. Dai, Antibacterial properties of magnesium in vitro and in an in vivo model of implant-associated methicillin-resistant Staphylococcus aureus infection, Antimicrob. Agents Chemother. 58 (2014) 7586, https://doi.org/10.1128/AAC.03936-14.

[81] K. Demishtein, R. Reifen, M. Shemesh, Antimicrobial properties of magnesium open opportunities to develop healthier food, Nutrients 11 (2019), https://doi.org/10.3390/NU11102363.

[82] Y. He, S. Ingudam, S. Reed, A. Gehring, T.P. Strobaugh, P. Irwin, Study on the mechanism of antibacterial action of magnesium oxide nanoparticles against foodborne pathogens, J. Nanobiotechnol. 14 (2016) 1–9, https://doi.org/10.1186/S12951-016-0202-0/FIGURES/6.

[83] P. Pham, S. Oliver, E.H.H. Wong, C. Boyer, Effect of hydrophilic groups on the bioactivity of antimicrobial polymers, Polym. Chem. 12 (2021) 5689–5703, https://doi.org/10.1039/D1PY01075A.

[84] A.M. Emelyanenko, A.G. Domantovsky, V.v. Kaminsky, I.S. Pytskii, K. A. Emelyanenko, L.B. Boinovich, The mechanisms of antibacterial activity of magnesium alloys with extreme wettability, Materials 14 (2021), https://doi.org/10.3390/MA14185454/S1.

[85] Z. Li, X. Gu, S. Lou, Y. Zheng, The development of binary Mg-Ca alloys for use as biodegradable materials within bone, Biomaterials 29 (2008) 1329–1344, https://doi.org/10.1016/J.BIOMATERIALS.2007.12.021.

[86] X. Gu, Y. Zheng, Y. Cheng, S. Zhong, T. Xi, In vitro corrosion and biocompatibility of binary magnesium alloys, Biomaterials 30 (2009) 484–498, https://doi.org/10.1016/J.BIOMATERIALS.2008.10.021.

[87] X. Lin, L. Tan, Q. Zhang, K. Yang, Z. Hu, J. Qiu, Y. Cai, The in vitro degradation process and biocompatibility of a ZK60 magnesium alloy with a forsterite-containing micro-arc oxidation coating, Acta Biomater. 9 (2013) 8631–8642, https://doi.org/10.1016/J.ACTBIO.2012.12.016.

[88] C.A. Schneider, W.S. Rasband, K.W. Eliceiri, NIH Image to ImageJ: 25 years of image analysis, Nat. Methods 9 (7) (2012) 671–675, https://doi.org/10.1038/nmeth.2089, 9 (2012).

[89] A.W. James, Review of signaling pathways governing MSC osteogenic and adipogenic differentiation, Scientifica (Cairo) (2013) 1–17, https://doi.org/10.1155/2013/684736, 2013.

[90] V.F. Bizelli, E.U. Ramos, A.S.C. Veras, G.R. Teixeira, L.P. Faverani, A.P.F. Bassi, Calvaria critical size defects regeneration using collagen membranes to assess the osteopromotive principle: an animal study, Membranes 12 (2022) 461, https://doi.org/10.3390/MEMBRANES12050461, 12 (2022) 461.

[91] A.P.F. Bassi, V.F. Bizelli, T.M. Francatti, A.C.R. de Moares Ferreira, J.C. Pereira, H.M. Al-Sharani, F. de A. Lucas, L.P. Faverani, Bone regeneration assessment of polycaprolactone membrane on critical-size defects in rat calvaria, Membranes 11 (2021) 124, https://doi.org/10.3390/MEMBRANES11020124, 11 (2021) 124.

[92] A.P.F. Bassi, V.F. Bizelli, L.F. de Mendes Brasil, J.C. Pereira, H.M. Al-Sharani, G.A. C. Momesso, L.P. Faverani, F. de A. Lucas, Is the bacterial cellulose membrane feasible for osteopromotive property? Membranes 10 (2020) 230, https://doi.org/10.3390/MEMBRANES10090230, 10 (2020) 230.

[93] P. Rider, Ž.P. Kačarević, A. Elad, D. Tadic, D. Rothamel, G. Sauer, F. Bornert, P. Windisch, D.B. Hangyási, B. Molnar, E. Bortel, B. Hesse, F. Witte, Biodegradable magnesium barrier membrane used for guided bone regeneration in dental surgery, Bioact. Mater. 14 (2022) 152–168, https://doi.org/10.1016/J.BIOACTMAT.2021.11.018.

[94] P. Rider, Ž.P. Kačarević, A. Elad, D. Rothamel, G. Sauer, F. Bornert, P. Windisch, D. Hangyási, B. Molnar, B. Hesse, F. Witte, Analysis of a pure magnesium membrane degradation process and its functionality when used in a guided bone regeneration model in beagle dogs, Materials 15 (2022) 3106, https://doi.org/10.3390/MA15093106, 15 (2022) 3106.

[95] M. Barbeck, L. Kühnel, F. Witte, J. Pissarek, C. Precht, X. Xiong, R. Krastev, N. Wegner, F. Walther, O. Jung, Degradation, bone regeneration and tissue response of an innovative volume stable magnesium-supported GBR/GTR barrier membrane, Int. J. Mol. Sci. 21 (2020) 3098, https://doi.org/10.3390/IJMS21093098, 21 (2020) 3098.

[96] D. Rothamel, F. Schwarz, A. Sculean, M. Herten, W. Scherbaum, J. Becker, Biocompatibility of various collagen membranes in cultures of human PDL fibroblasts and human osteoblast-like cells, Clin. Oral Implants Res. 15 (2004) 443–449, https://doi.org/10.1111/J.1600-0501.2004.01039.X.

[97] J. Wang, Y. Qu, C. Chen, J. Sun, H. Pan, C. Shao, R. Tang, X. Gu, Fabrication of collagen membranes with different intrafibrillar mineralization degree as a potential use for GBR, Mater. Sci. Eng. C 104 (2019), 109959, https://doi.org/10.1016/J.MSEC.2019.109959.

[98] L. Dupoirieux, D. Pourquier, M.C. Picot, M. Neves, Comparative study of three different membranes for guided bone regeneration of rat cranial defects, Int. J.

Oral Maxillofac. Surg. 30 (2001) 58–62, https://doi.org/10.1054/IJOM.2000.0011.
[99] D. Rothamel, F. Schwarz, M. Sager, M. Herten, A. Sculean, J. Becker, Biodegradation of differently cross-linked collagen membranes: an experimental study in the rat, Clin. Oral Implants Res. 16 (2005) 369–378, https://doi.org/10.1111/J.1600-0501.2005.01108.X.
[100] Y.Z. An, Y.K. Kim, S.M. Lim, Y.K. Heo, M.K. Kwon, J.K. Cha, J.S. Lee, U.W. Jung, S.H. Choi, Physiochemical properties and resorption progress of porcine skin-derived collagen membranes: in vitro and in vivo analysis, Dent. Mater. J. 37 (2018) 332–340, https://doi.org/10.4012/DMJ.2017-065.
[101] A. Vajgel, N. Mardas, B.C. Farias, A. Petrie, R. Cimões, N. Donos, A systematic review on the critical size defect model, Clin. Oral Implants Res. 25 (2014) 879–893, https://doi.org/10.1111/CLR.12194.
[102] C. Chu, L. Liu, Y. Wang, S. Wei, Y. Wang, Y. Man, Y. Qu, Macrophage phenotype in the epigallocatechin-3-gallate (EGCG)-modified collagen determines foreign body reaction, J. Tissue Eng. Regen. Med. 12 (2018) 1499–1507, https://doi.org/10.1002/term.2687.
[103] C. Chu, Y. Wang, Y. Wang, R. Yang, L. Liu, S. Rung, L. Xiang, Y. Wu, S. Du, Y. Man, Y. Qu, Evaluation of epigallocatechin-3-gallate (EGCG) modified collagen in guided bone regeneration (GBR) surgery and modulation of macrophage phenotype, Mater. Sci. Eng. C 99 (2019) 73–82, https://doi.org/10.1016/j.msec.2019.01.083.
[104] C. Chu, S. Rung, Y. Wang, Y. Qu, Y. Man, Comment on " in situ mannosylated nanotrinity-mediated macrophage remodeling combats Candida albicans infection,", ACS Nano 15 (2021) 3541–3543, https://doi.org/10.1021/acsnano.0c07851.
[105] B. Allan, R. Ruan, E. Landao-Bassonga, et al., Collagen membrane for guided bone regeneration in dental and orthopedic applications, Tissue Eng. 27 (5–6) (2021) 372–381, https://doi.org/10.1089/ten.TEA.2020.0140.
[106] B. Wessing, S. Lettner, W. Zechner, Guided bone regeneration with collagen membranes and particulate graft materials: a systematic review and meta-analysis, Int. J. Oral Maxillofac. Implants 33 (1) (2018) 87–100, https://doi.org/10.11607/jomi.5461.
[107] R. Lo Nigro, E. Schilirò, G. Mannino, S. Di Franco, F. Roccaforte, Comparison between thermal and plasma enhanced atomic layer deposition processes for the growth of HfO2 dielectric layers, J. Cryst. Growth 539 (2020), 125624, https://doi.org/10.1016/j.jcrysgro.2020.125624.
[108] P. Poodt, D.C. Cameron, E. Dickey, S.M. George, V. Kuznetsov, G.N. Parsons, F. Roozeboom, G. Sundaram, A. Vermeer, Spatial atomic layer deposition: a route towards further industrialization of atomic layer deposition, J. Vac. Sci. Technol. A Vacuum, Surfaces, Film. 30 (2012), 010802, https://doi.org/10.1116/1.3670745.
[109] M. Doulberis, A. Papaefthymiou, S.A. Polyzos, et al., Rodent models of obesity, Minerva Endocrinol. 45 (3) (2020) 243–263, https://doi.org/10.23736/S0391-1977.19.03058-X.
[110] M. Kleinert, C. Clemmensen, S.M. Hofmann, et al., Animal models of obesity and diabetes mellitus, Nat. Rev. Endocrinol. 14 (3) (2018) 140–162, https://doi.org/10.1038/nrendo.2017.161.